International Journal of Multiphase Flow 000 (2018) 1–21

Contents lists available at ScienceDirect

International Journal of Multiphase Flow

journal homepage: www.elsevier.com/locate/ijmulflow

Study of bubbles entrapped into a gas-sheared liquid film

David B. Hann[a,*], Andrey V. Cherdantsev[b,c], Barry J. Azzopardi[a]

[a] Faculty of Engineering, University of Nottingham, Nottingham, UK
[b] Kutateladze Institute of Thermophysics, Novosibirsk, Russia
[c] Novosibirsk State University, Novosibirsk, Russia

ARTICLE INFO

Article history:
Received 22 January 2018
Revised 18 May 2018
Accepted 2 July 2018
Available online xxx

Keywords:
Gas-sheared liquid film
Disturbance waves
Bubble entrapment
Bubble size
Bubble velocity
Laser-induced fluorescence

ABSTRACT

The surface of a thick liquid film under strong gas shear is covered by large-scale disturbance waves and small-scale ripples. Disruption of these ripples on top of disturbance waves by the gas stream leads to the creation of droplets that are entrained into the gas core and may deposit back onto the film surface. In addition, gas may be entrapped by the liquid film in the form of bubbles of various sizes. In this work, the study of gas bubble creation was performed in a horizontal rectangular duct using the brightness-based laser-induced fluorescence technique. With this technique, the instantaneous height of the liquid film was measured with a 40 µm spatial resolution over a 51 mm by 20 mm area at speeds of 10 kHz. The entrapped bubbles and entrained/depositing droplets are detectable in the data and can thus be studied simultaneously with the waves on the film surface. Several scenarios of bubble entrapment and collapse were identified and discussed. The dynamics of entrapped bubbles was studied quantitatively using an automatic processing algorithm, confirming and elucidating the results of qualitative observations. The effect of the flow parameters on the bubbles concentration, velocity and size distributions was studied separately for the bubbles inside the disturbance waves and inside the thin base film between the disturbance waves. It was shown that the bubbles are mostly created due to oblique impacts of droplets at the base film and are accumulated by the disturbance waves. A small number of bubbles of larger size are created in front of disturbance waves and remain inside the disturbance waves. The velocity of the bubbles is affected by the velocity of the surrounding liquid. Using the bubbles as tracers, a profile of longitudinal liquid velocity was constructed and a noticeable increase of wall shear under the rear slopes of disturbance waves was found.

1. Introduction

Annular flow is the multiphase flow regime where a thin film of liquid is carried along the channel walls by a high velocity gas stream which flows along the centre of a channel. At large enough gas and liquid flow rates, liquid droplets are torn from the film surface and entrained into the core gas stream. This flow is characterised by high rates of heat and mass transfer due to a high degree of turbulent mixing and a large interfacial area. Therefore annular flow is widely used in heat exchangers, cooling systems and chemical industry; it also occurs in production and transportation pipelines in oil-and-gas industry, steam generators and evaporators. Large interfacial area is achieved in this flow due to a number of factors, related to each other. Three kinds of gas-liquid interface exist in annular flow: 1) Surface of liquid film covered by complicated system of waves, 2) Surface of droplets entrained into the gas core; 3) Surface of gas bubbles entrapped into the liquid film.

1.1. Film wavy structure

The film surface is covered by large-scale structures called "disturbance waves" or "roll waves". These large lumps of liquid travel with high velocity across a thin residual layer of liquid called a "base film" without changing significantly over long distances (Hall Taylor et al., 1963). The surface of both the disturbance waves and the base film is covered by small-scale "ripples". All the ripples are generated at the rear slopes of the disturbance waves (Alekseenko et al., 2008) and either decelerate and travel across the base film ("slow ripples") or accelerate and travel across the top parts of "parent" disturbance waves ("fast ripples"). Both the longitudinal and transverse size of slow and fast ripples are at least an order of magnitude smaller than that of disturbance waves. At the same time, the fast ripples are characterised by higher amplitudes and steeper slopes than the slow ones, thus making

---

[*] Corresponding author.
E-mail address: david.hann@nottingham.ac.uk (D.B. Hann).

https://doi.org/10.1016/j.ijmultiphaseflow.2018.07.001
0301-9322/

the surface of disturbance waves much rougher than that of the base film. Both slow and fast ripples are three-dimensional in shape. In particular, the fast ripples noted in both horizontal rectangular ducts and upward flow in a circular duct are horseshoe-shaped and placed on top of disturbance waves in a staggered order (Cherdantsev et al., 2014). Strong similarities are noted in both configurations. The slow ripples end by being absorbed when the following disturbance wave overtakes them. The fast ripples either disappear due to decay at the front of the parent disturbance wave or due to being scattered by the gas stream into droplets. This scattering is the main source of primary entrainment of liquid from film surface in annular flow.

1.2. Droplet entrainment and deposition

The detachment of the droplets from film surface occurs via the formation of two kinds of transitional liquid structures, called "liquid bags" and "liquid ligaments" (Azzopardi, 1983; Pham et al., 2014). According to Cherdantsev et al. (2014), bag break-up occurs when the whole front of a fast ripple is blown-up by the gas stream (see also Woodmansee & Hanratty, 1969), whilst ligament break-up occurs at a junction of side edges of two adjacent fast ripples. After a break-up of any kind, a number of droplets are created with a wide range of sizes and velocities.

Both the longitudinal and transverse velocity components of entrained droplets just after impact are of order of a few metres per second (Azzopardi, 1987; Alekseenko et al., 2014). The longitudinal component increases with time due to the action of gas drag force (Azzopardi & Teixeira, 1994; Fore & Dukler, 1995; Zaidi et al., 1998). The transverse velocity component is conserved for droplets larger than 0.2 mm (James et al., 1980). In horizontal / inclined flows, the droplets also gain an accelerating transverse velocity component due to the action of gravity. The movement in the transverse direction will cause the droplets to eventually reach a film surface and impact it at an oblique angle.

Cherdantsev et al. (2017) observed three scenarios of impact of a droplet depositing from the gas core onto a gas-sheared liquid film. In one of the cases, which most often occurs at thin films with low interfacial slopes, - i.e., on the base film surface - the impacting droplet creates long and narrow "furrow" on film surface. Similar events were observed by Okawa et al. (2008) who studied the oblique droplet impact onto static liquid surface. The film surface behind the protruding droplet becomes covered with very short transversely oriented waves, probably appearing due to a strong shear induced by the passing droplet and related Kelvin-Helmholtz instability. The most interesting phenomenon during such an impact (not reported by Okawa et al., 2008) is the massive entrapment of gas bubbles behind the protruding droplet.

1.3. Gas bubbles entrapped by liquid film

If the entrained droplets in the gas core are often referred to as "the third phase", the first two being the gas core and liquid film, the bubbles can be referred to as "the fourth phase". The presence of numerous bubbles is reported in many experimental papers in which visualisation of gas-sheared liquid film was employed. These studies include visualisation in the plane of the wall (Hewitt & Roberts, 1969; Woodmansee & Hanratty, 1969; Van Nimwegen et al., 2015; Dasgupta et al., 2017) and in the plane of the duct's longitudinal section (Hewitt et al., 1990; Schubring et al., 2010; Zadrazil et al., 2014; Pan et al., 2015) with various optical methods. The gas bubbles inside the liquid film are expected to play important role in the flow hydrodynamics. The presence of bubbles may change the overall effective hydrodynamic parameters of liquid film such as density and viscosity. Bubbles contribute to an increase in the interfacial area and thus may enhance chemical reactions. Between an entrapped bubble and the duct's wall an area of locally much thinner film exists and, consequently, a much higher heat transfer rate appears (Mesler, 1976). The initiation of nucleate boiling by passing disturbance waves noted by Barbosa et al. (2003) could be explained by gas bubbles entrapped in the disturbance waves and acting as nucleation sites if they adhered to the wall of the duct. The bursting of entrapped bubbles is supposed to be one of the mechanisms of droplet entrainment (Hewitt & Hall Taylor, 1970; Ishii & Grolmes, 1975). The presence of bubbles may also affect the reliability of film thickness measurements in annular flow. When measuring using the conductivity method, a significant quantity of bubbles could produce a weaker conductance and so produce an under-prediction of the film thickness (van der Meulen, 2011). When measuring using optical techniques based on light reflection such as Laser Focus Displacement technique (Hazuku et al., 2008), the bubbles interfaces may be interpreted as the film interface and also cause under-prediction of the real film thickness.

Despite their importance, bubbles in annular flow have not been studied as intensively as waves on film surface or entrained droplets. Nearly the only paper specifically devoted to studying the bubbles in annular flow was the paper by Rodriguez & Shedd (2004a), who measured the number and sizes of entrapped bubbles in horizontal pipe with inner diameter of 15.1 mm at three different circumferential positions. A backlit visualisation technique was employed with an outstanding spatial resolution (4.2 µm/pixel) and decent exposure time (30 µs), but with low sampling frequency which prevented them from studying the bubbles dynamics. As a result, only distributions of bubbles by size normalised by base film thickness were obtained. The distributions were described by a monotonically decaying exponential function; it was shown that the bubbles sizes decrease with increase in gas velocity. Unfortunately, the measurements were conducted only inside the base film due to strong redistribution of light by rough surface of the disturbance waves which caused significant errors in the processing algorithm. This limitation will bias the results to smaller bubble sizes and concentrations, since large bubbles are seen to be carried by the disturbance waves.

Kopplin (2004) followed this work by measuring the axial and circumferential velocities of the entrapped bubbles. He assumed that the entrapped bubbles act as tracers and allow measurements of local liquid velocity inside the film. The data was taken separately inside smooth areas of the base film, inside the ripples on the base film and inside the disturbance waves. It was shown that inside ripples and disturbance waves the velocity variation increases. Zadrazil et al. (2014) used Planar LIF technique to study statistical characteristics of waves on film surface in annular flow. They also paid attention to measuring the bubbles frequency and size distribution. These characteristics were found to be linked to the interfacial roughness, and it was thus suggested that gas entrainment is related to the existence of large-amplitude waves.

In their visualisation study, Woodmansee and Hanratty (1969) focused on the process of liquid entrainment. They have also noticed that the bubbles are accumulated inside the disturbance waves and suggested that the bubbles are entrapped when "*ripples once lifted from the interface fall forward onto the liquid film*". Based on their PLIF visualisation, Rodriguez & Shedd (2004b) assumed that "*folding*" of disturbance waves crests leads to the formation of pockets of air trapped inside the film. These and further discussion on the mechanisms of bubbles entrapment is given in Section 3.1.

1.4. The goal and structure of the paper

The goal of the present paper is a comprehensive and systematic investigation of gas bubbles trapped by gas-sheared liquid film

Please cite this article as: D.B. Hann et al., Study of bubbles entrapped into a gas-sheared liquid film, International Journal of Multiphase Flow (2018), https://doi.org/10.1016/j.ijmultiphaseflow.2018.07.001

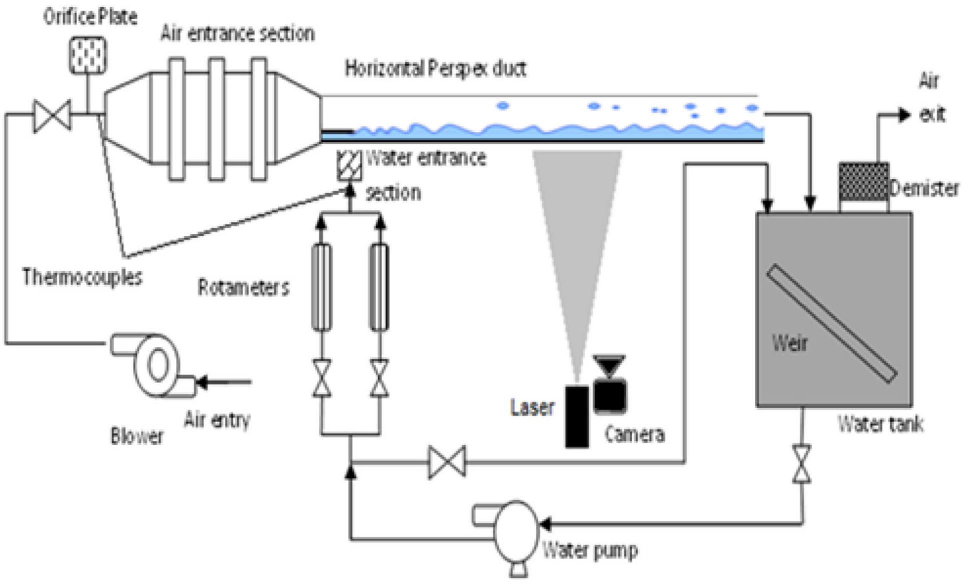

Fig. 1. Schematic showing the configuration of the shearing rig and associated measurement system.

in annular gas-liquid flow. Such a study should be conducted on two levels. Firstly, it should yield qualitative understanding of all stages of evolution of a single bubble, starting from its entrapment and ending by its collapse. Secondly, it should present quantitative characterisation of as large a number as possible of bubbles that are present in real gas-sheared film in terms of their concentration and distributions by size and velocity at different flow conditions. Since both evolution and properties of the bubbles are expected to be affected by the disturbance waves, both qualitative and quantitative studies should be conducted with relation to presence of disturbance waves in the area of interrogation. This connection is one of the reasons why the measurements of bubbles properties should be conducted simultaneously with field measurements of local film thickness in the whole area of interest. This goal will be achieved using Brightness-Based Laser-Induced Fluorescence (BBLIF) technique. The paper is structured as follows. Section 2 describes the experimental set-up, film thickness measurements technique and the algorithm of automatic detection of entrapped bubbles in BBLIF data. Section 3 describes the results of an extended qualitative study of mechanisms of bubbles entrapment and scenarios of bubbles collapse, together with comparison of the results to the qualitative observations from literature. Section 4 presents the results of an analysis of bubbles size distributions and concentration. Section 5 presents analysis of bubbles velocity and an attempt to characterise the velocity profile inside the liquid film using bubbles as traces, similar to analysis of Kopplin (2004), but with relation to the film thickness. The final section summarises the results.

2. Experimental details

2.1. Experimental setup and measurement technique

The experiments were carried out in the shearing rig which is part of the Multiphase research group at the University of Nottingham. This rig is the same as used by Alghoul et al. (2011) and Cherdantsev et al. (2014, 2017) and a schematic of the shearing rig is shown in Fig. 1. The working section of the rig is a horizontally-oriented rectangular duct of 0.025 m height, 0.161 m width and 2 m length. The air is supplied by the blower, being introduced through a conditioning section and a honeycomb grid. The flow rate of the air is controlled and monitored with reference to a calibrated orifice plate to determine the mean flow rate through the system. Water is introduced at the base of the duct and the flow rate is monitored with a calibrated flowmeter. The gas flow pushes the liquid along the section until it is discharged from the separator. From previous results it is known that air flow rates corresponding to gas superficial velocities of 25, 30 and 35 m/s and liquid Reynolds numbers of 220, 360 and 520 result in droplet entrainment, and these values were chosen for further study. In this case the liquid Reynolds number was defined as the volumetric liquid flow rate per unit width of the duct ("loading factor", L_f) divided by the kinematic viscosity of liquid, $Re_L = L_f/\nu$, and the gas superficial velocity, V_G, is the volumetric flow rate of the air divided by the cross-sectional area of the duct. Tap water is used as working liquid.

The Brightness-Based Laser-Induced Fluorescence (BBLIF) technique is used because it can provide field measurement of local film thickness. The method employs the Lambert-Beer law integrated over a layer of liquid containing a fluorescent dye to monotonically correlate the thickness of the layer to the brightness of fluorescence (Hidrovo & Hart, 2001). The fluorescent dye (Rhodamine 6G) is dissolved in the working liquid in small (15 mg/l) concentration and excited by illuminating the working liquid by laser light with a wavelength of 527 nm, which is close to the maximum in absorption spectrum of the dye. The irradiated light is re-emitted in the red spectral domain and its intensity can be measured with a camera equipped by low-pass optical filter to remove the laser wavelengths. The recalculation formula together with calibration procedure can be found in Cherdantsev et al. (2017).

Both camera and laser were located below and pointing upwards at the bottom of the duct at the distance of 1.6 m from the inlet (37 duct hydraulic diameters). The laser beam was expanded over an area to obtain the instantaneous shape of film surface resolved in both longitudinal and transverse coordinate within the Region of Interest (*RoI*) which was 51 mm in longitudinal direction, x, and 20 mm (1/8 of the width of the duct) in transverse direction, y. This size of *RoI* yielded spatial resolution of 40 µm/pixel and provided a balance between the need to view as large an area as possible and the need to see small features. The laser was pulsed at its maximum rate of 10 kHz and the camera was synchronised with the laser. The exposure time was defined by the laser pulse duration and was approximately 10^{-7} s. For each combination of flow rates three records of 2000 images (which corresponds to duration

Please cite this article as: D.B. Hann et al., Study of bubbles entrapped into a gas-sheared liquid film, International Journal of Multiphase Flow (2018), https://doi.org/10.1016/j.ijmultiphaseflow.2018.07.001

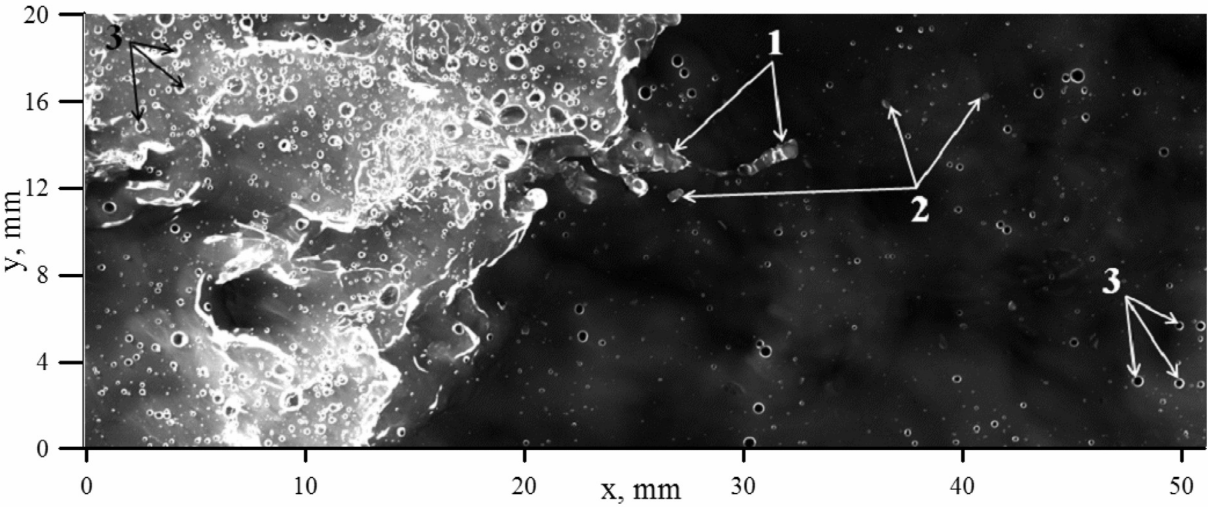

Fig. 2. An example of BBLIF data: instantaneous matrix $h(x,y)$ in graphical form. $Re_L = 520$, $V_G = 30$ m/s. Numbers denote: liquid ligament (1), liquid droplets (2) and entrapped bubbles (3).

of 0.2 s) were obtained. As a result, the data were obtained in the form of three-dimensional matrices $h(x,y,t)$, where h is local film thickness.

2.2. Understanding different objects in BBLIF data

The value of the film thickness, $h(x,y,t)$, obtained by the BBLIF technique, corresponds to real local film thickness, h_{real}, under two conditions. The first condition is that the slope of the interface in the point of measurement, $\mathrm{d}h_{\mathrm{real}}/\mathrm{d}x$ and $\mathrm{d}h_{\mathrm{real}}/\mathrm{d}y$, should not be larger than a critical angle. Steep slopes cause an increase in the reflection coefficient: for water-air interface a significant increase starts around 35°–40° and total internal reflection occurs at about 48°. The additional illumination caused by the reflected laser light is not taken into account by the recalculation procedure and causes a non-physical increase in the measured local film thickness.

The second condition is that the optical beam along which the brightness is collected by a single pixel of the camera, should cross only one gas-liquid interface. In such a case only one continuous layer of liquid, namely, the liquid film on the duct's bottom, contributes to the measured brightness of fluorescence. In real gas-sheared film flow, with droplet entrainment and bubbles entrapment, other cases are possible. One example of a situation when this condition is broken is the probable overturning of fast ripple waves or formation of liquid bags/ligaments, when the optical beam first crosses the liquid film at the wall and then the liquid structure "hanging" above it.

Another example is that of a droplet, flying above the film surface. Since such a droplet was entrained from liquid film surface, it contains fluorescent matter and it is also illuminated by the laser light which has passed through the film. Thus, such droplet would contribute towards the local brightness of fluorescence and the local film thickness will be calculated based on total brightness emitted by both the film and the droplet. Thus, droplets appear in BBLIF data as localised spots of higher "film thickness", moving with very high speed. The value of $h(x,y,t)$ inside the droplet location does not necessarily correspond to the sum of film thickness and droplet height, since the laser light illumination inside the droplet may be non-uniform due to curvilinear surface of the droplet, especially if the droplet is of elliptic shape (Alekseenko et al., 2014).

The trapped bubbles, on the other hand, do not contain the fluorescent matter. Thus, their presence would reduce the local brightness of fluorescence and, hence, local measured "film thickness". At the bubble's periphery the incident light will inevitably meet the water-air interface at steep slopes of up to 90°, which will cause total internal reflection of the incident light. Thus, as described above, at the border of a bubble, a narrow ring of very high apparent "film thickness" will be calculated by BBLIF algorithm.

An example of a matrix of "film thickness", $h(x,y)$, at a fixed moment of time is presented in Fig. 2 in a graphical form. In this processed image, the local brightness of each pixel of the image is linearly proportional to the local value of $h(x,y)$. In this scale, white corresponds to a film thickness of 2 mm. The flow direction is from left to right and the left of the image is brighter due to the front part of a disturbance wave; to the right it is darker because it represents the base film surface in front of it. The arrows mark a liquid ligament (1), entrained droplets (2) and bubbles (3).

It is obvious from Fig. 2 that the number of bubbles inside the disturbance waves is much larger than that inside the base film. This difference is not only related to the thicker film inside the disturbance wave: the number of bubbles per unit wall area also increases significantly. In addition, larger bubbles can be encountered among the smaller bubbles inside the disturbance waves.

2.3. Algorithm of bubbles identification

The algorithm of automatic identification for entrapped bubbles is based on several observations. First, the typical size of a bubble is much smaller than the size of both fast and slow ripples, not to mention the disturbance waves. Thus, the waves and the bubbles can be separated based on spatial scale. Second, the shape of a bubble in BBLIF data has distinctive features such as a "cavity" in the centre and high ridgelines around it. These features make the bubbles easier to identify and discriminate from droplets compared to standard imaging techniques.

Fig. 3 illustrates the main steps of the algorithm applied to a small fragment of BBLIF data.

- The original image (Fig 3a) was segmented into a low (Fig 3b) and high frequency (Fig 3c) component using the median of the image taken over a square with side of 50 pixels (2 mm). This segmentation estimates the local film height around the bubble from the local median values (Fig. 3b) and identified the high frequency components associated with the bubbles, droplets and other features as the difference between the original and the median-filtered image (Fig. 3c).
- The high-frequency image of the bubble contained a depression surrounded by a brighter ring as shown in Fig. 3c. Unfor-

Please cite this article as: D.B. Hann et al., Study of bubbles entrapped into a gas-sheared liquid film, International Journal of Multiphase Flow (2018), https://doi.org/10.1016/j.ijmultiphaseflow.2018.07.001

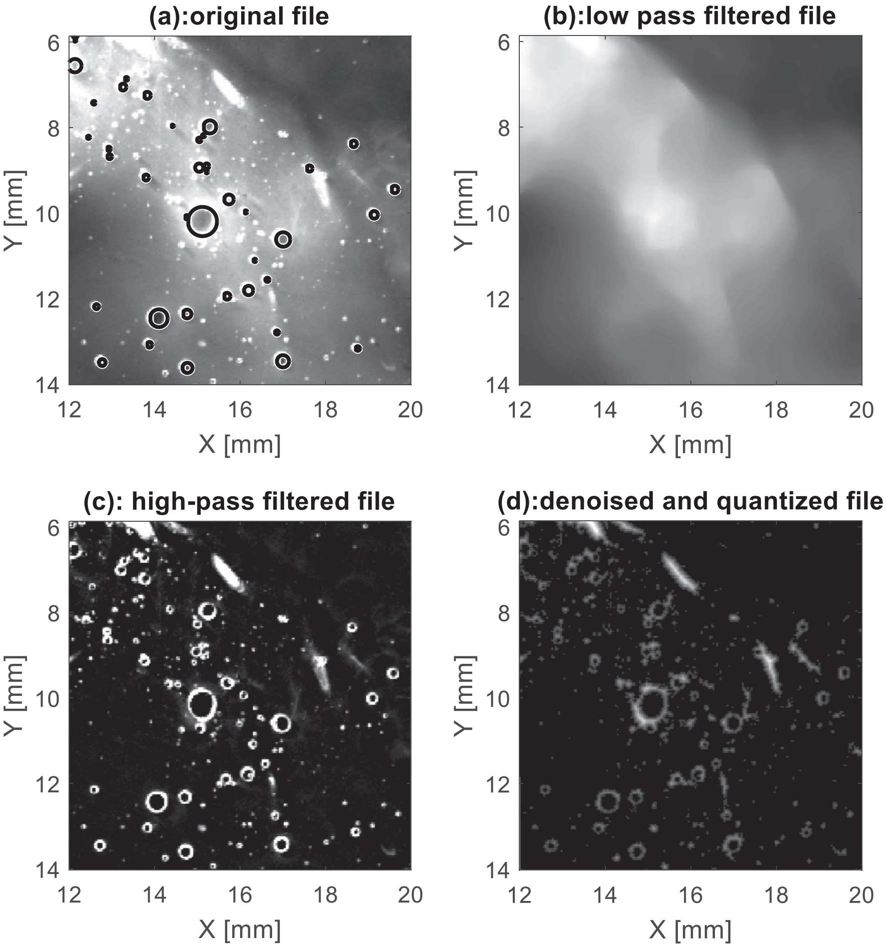

Fig. 3. Example of the stages of the analysis algorithm: (a) small segment of larger image with identified bubbles present; (b) low pass median filter of the data (50×50); (c) high-pass median filtered data showing variation of the film; (d) quantised image to minimise over-segmentation in the watershed.

tunately, this is only true for bubbles larger than double spatial resolution (i.e., about 80 μm) in diameter, so smaller bubbles are ignored in this analysis. The images were quantised by decreasing the number of levels from 256 to 16 to prevent over-segmentation due to noise levels during the detection of catchment areas (Fig. 3d) and then a watershed analysis (Matlab 2017b) was used to detect the depressions associated with bubbles. For each of these watershed regions bordered by the maximum of the rim, the equivalent diameter and centroid were recorded.

- Regions with large eccentricity $\epsilon > 2$ or over 1000 pixels in size (over 1.42 mm in diameter) were filtered out as being associated with the space between bubbles or optical distortions.
- The velocity of the bubbles was measured using a particle tracker algorithm that used the centroids of the identified bubbles. This algorithm used a modification of the Hungarian linker algorithm (Cao, 2008) which uses the Munkres function (Munkres, 1957) to identify if a bubble pair exists in adjacent frames. A size discriminator was also implemented to ensure only a bubble of comparative size was matched between image pairs. If no pair existed in adjacent frames then the bubble was marked as false and was not counted as a true bubble. This step was used as a final filter to ensure only real bubbles were counted. As can be seen from Fig. 3a, this clearly identified most of the bubbles larger than 2 pixels in size. Obviously it undercounted the smallest bubbles, so these are ignored in the further analysis. The method also easily discriminated between droplets and bubbles due to absence of a prominent depression of brightness in droplet's central part and much larger velocity of the droplets; so no droplets were counted.

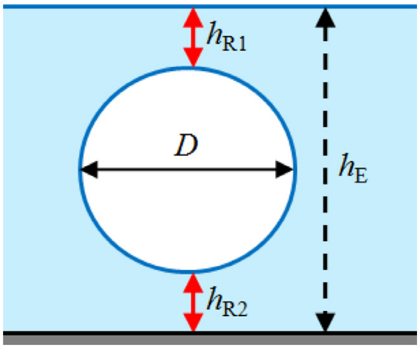

Fig. 4. A drawing illustrating definition of the quantities h_E and $h_R = h_{R1} + h_{R2}$.

2.4. Measurable quantities and measurement errors

The quantities being measured to characterise a single bubble at each time instant are: the coordinates of its centroid, x and y, its equivalent diameter in x-y plane, D, and its velocity, V. In addition, two quantities characterising the bubble in z-direction can be estimated. The first quantity is the thickness of liquid film encompassing the bubble, h_E. The idea is illustrated in a sketch (see Fig. 4), in which h_E is equal to the length of the vertical dashed

Please cite this article as: D.B. Hann et al., Study of bubbles entrapped into a gas-sheared liquid film, International Journal of Multiphase Flow (2018), https://doi.org/10.1016/j.ijmultiphaseflow.2018.07.001

line. In the experiments, h_E is estimated as the median film thickness in a 2 mm x 2 mm area around the centre of the bubble. The second quantity is the thickness of the residual liquid film both under and above the bubble, h_R, equal to the sum of the lengths h_{R1} and h_{R2} in Fig. 4. In the experiments this quantity is estimated as a local film thickness value in the centre of the bubble.

To characterise the overall behaviour of bubbles, the number of bubbles detected in each image and the average film thickness over each image were measured. The uncertainty in the bubble velocity and location are mostly related to pixelisation. The location is determined by the centroid algorithm, so it could be estimated to sub-pixel accuracy. The velocity will therefore have an uncertainty related to the magnitude of the displacement between images. This uncertainty would be about 20% for velocities of the order of 0.2 m/s, dropping to 4% for velocities of 1 m/s. The size of the bubbles is calculated using the equivalent diameter algorithm, with uses the area of the often elliptical bubbles to determine an equivalent diameter if the area was a circle. For example, a 0.1 mm bubble would have an uncertainty of 8% while for a bubble of 0.3 mm the uncertainty would be of the order of 1%.

The known issues with film thickness measurements are described in Section 2.2. If the local film slope is not large and there is only one interface seen in the considered pixel, there are no significant distortions. In this case the error in film thickness measurements is mostly defined by the camera noise and does not exceed 5%. Many of the distortion sources are of small size and so can be segmented from the main image by the use of a 2D-median filter prior to calculation of film thickness. If the size of a distortion source - such as a bubble or a droplet - is smaller than half of the filter window area, then the median filter will provide a value that is representative of the most probable value of the height of the film surrounding the feature. In this application the mean bubble sizes are of the order of 300 µm, corresponding to an area of 44 pixels, which is significantly less than that of the filtering window (50 by 50). This estimation assumes that the adjacent features do not interpose.

To test the segmentation process, sample images were analysed to ascertain the validity of detection. The proportion of correct identifications from the watershed segmentation were 95%. In other words, we have a confidence in 95% of all the values given and only 5% of the values are false positives. However, to achieve this confidence in the measured values, it was necessary to set harsh conditions, which resulted in a relatively high number of false negatives. Thus, the number of bubbles detected was less than the number of bubbles present; about 15% of the bubbles in the disturbance waves were ignored in this analysis. The detection rate for bubbles larger than 80 µm in the base film was also very high. However, it can be observed that there were a significant number of very small bubbles that are not detected and this will affect the later statistics.

3. Evolution of the bubbles: entrapment and collapse

The goal of the first stage of this study is to understand the physical mechanisms responsible for entrapment of air inside the liquid film and for air release. For this purpose, the qualitative analysis started in Cherdantsev et al. (2017) of the processes of generation is expanded to include other mechanisms and an analysis of the extinction of bubbles is performed.

3.1. Mechanisms of bubbles entrapment

In the present study, we have managed to visually detect three repeatable mechanisms of bubbles entrapment noted from close analysis of all of the videos:

- Entrapment due to "furrow" impact of depositing droplets, first observed by Cherdantsev et al. (2017), this will be expanded in more detail here,
- Entrapment due to the impact of remnants of transitional liquid structures, not reported previously;
- Entrapment due to overturning of fast ripple waves, observed by Woodmansee & Hanratty (1969) and Rodriguez & Shedd (2004b).

Sample examples of these mechanisms are illustrated and discussed below in the separate subsections.

3.1.1. Entrapment due to impacting droplets

As reported by Cherdantsev et al. (2017), massive entrapment of small bubbles into a gas-sheared liquid film occurs due to the impacts of droplets previously entrained from film surface. When these droplets deposit back at shallow angle of impact, they plough along the film surface, creating a highly-perturbed long and narrow "furrow" in their wake. An example of the BBLIF-record of this process is shown in Fig. 5 (see Video 1 for the full sequence). Prior to the impact of a droplet, the film surface was almost free of bubbles (a). After the first contact to the film surface, the impacting droplet moves along the surface, generating a furrow of a few centimetres long (b, c). After the droplet has passed, numerous entrapped bubbles are observed inside the liquid film (c).

The exact mechanism of bubbles entrapment during the "furrow" impact remains unclear. In the literature, several mechanisms of air entrainment due to droplet impact have been proposed, but none of them matches the observations in the present work. The most studied mechanism of this kind is trapping of thin gas disk ("air cushion") between the surfaces of a falling droplet and the pool (e.g. Thoroddsen et al., 2003; Korobkin et al., 2008; Hicks et al., 2012). The difference between this process and the "furrow" impact is in the volume of the entrapped air: during the furrow impact total volume of the entrapped bubbles may be comparable to the volume of the impacting droplet (see Fig. 5 in the present paper and Fig. 5 in Cherdantsev et al. (2017). In the air-cushioning entrapment process, the ratio of the volumes is usually less than 10^{-4} (Tran et al., 2013). Two other mechanisms were observed during droplet impact into a deep pool: entrapment of gas bubbles by the vortex ring forming around the impacting droplet (Caroll & Mesler 1981; Thoraval et al., 2016) or entrapment of a large bubble above the drop, penetrating the pool surface at high speed (Deka et al., 2017). During the "furrow" impact, the droplet remains near the film surface; besides, film thickness in the considered flow is comparable to the size of the impacting droplet and thus cannot be considered a deep pool.

Quite likely, the entrapment we observe is related to a strong deformation of either the liquid film, or impacting droplet surface, or both. In the modelling of oblique impact by Xie et al. (2017), the furrow seems to consist of a chain of craters on the film surface, although, no entrapped bubbles were observed inside the modelled film. In the model of Guo & Lian (2017) the upper part of the droplet moves faster than the lower part which appears to be adhered to the film surface. This difference may lead to the formation of gas pockets between the film and the upper part of the droplet. Hale & Akers (2016) experimented with relatively slow and large droplets moving almost horizontally over the liquid surface. Using tracer particles, they have detected rolling motion in the moving droplet, and this kind of motion may also be true for the faster droplets typical in annular flow which might also lead to bubbles entrapment.

Rodriguez & Shedd (2004b) cast doubt about the significance of droplet impacts in bubble creation for their experiments by noting that the bubbles density was much higher than the number of droplet impacts per unit time in the same area. This observation

Please cite this article as: D.B. Hann et al., Study of bubbles entrapped into a gas-sheared liquid film, International Journal of Multiphase Flow (2018), https://doi.org/10.1016/j.ijmultiphaseflow.2018.07.001

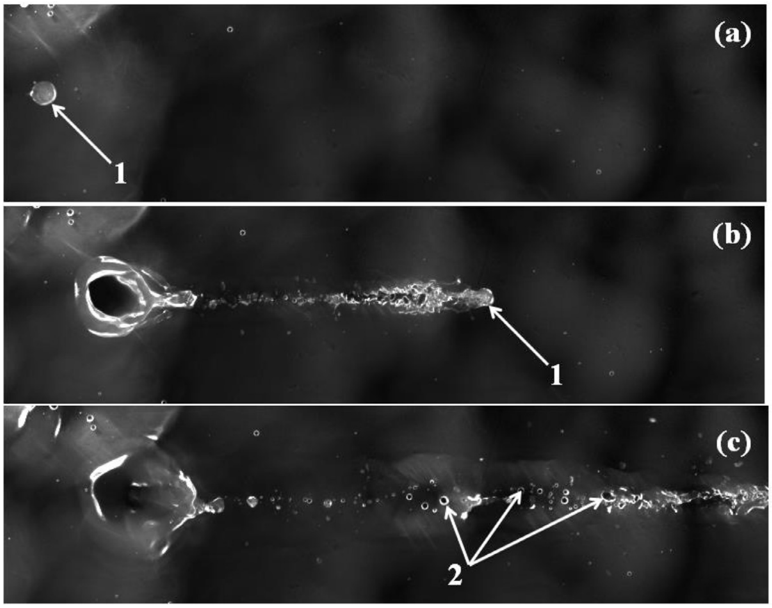

Fig. 5. Bubbles entrapment due to oblique droplet impact. The numbers denote: impacting liquid droplet (1); entrapped gas bubbles (2). $Re_L = 220$, $V_G = 25$ m/s. Image size is 31.2 mm by 8 mm. The time increases downwards with the time step of 1 ms.

does not disprove the discussed mechanism for two reasons: first, a single impacting droplet can create a large number of bubbles; second, some of the entrapped bubbles remain inside the film after the impact, thus, the bubbles are accumulated due to numerous impacts and their number grows with time and downstream distance.

These furrow impacts occur mainly on the base film behind the disturbance waves. This peculiarity is supposedly linked to the shallow angles of the slopes of slow ripple waves covering the base film. Droplet impacts is the only entrapment scenario that could happen on the base film far from the disturbance waves. The two other scenarios occur in front of the disturbance waves.

3.1.2. Impacts of the transitional structures

During visual inspection of the data, the creation of larger bubbles just in front of disturbance waves was observed. This occurs when the remnants of transitional entrainment structures – liquid bags or liquid ligaments – fall down onto the film. Such remnants may carry a significant mass of liquid, much larger than that typically carried in the droplets. An example of such an event is shown in Fig. 6 as a sequence of images with a time step of 2 ms. In this case, a lump of liquid (1), presumably part of a former liquid bag torn from disturbance wave (2), passes across the measurement area with speed of about 5 m/s, and a number of large bubbles (3) with sizes comparable to that of large bubbles inside the disturbance wave (4), are created. These bubbles are quite likely to survive, since the time they spend in the base film is relatively short and they are promptly overrun by the disturbance wave which created them. The full event is shown in Video 2. It is interesting to observe a long ditch (5) created by the remnant of the liquid lump (1). This ditch also turns into two large bubbles by the end of the sequence.

It could be expected that the physical mechanisms of bubbles creation by the droplets and by the larger lumps of liquid are the same, since the difference between the two cases is only quantitative, being defined by the size of the impacting object.

3.1.3. Entrapment due to overturning of the fast ripples

Other possible sources of bubbles generation are reported in different gas-liquid flows. These mechanisms include: gas entrapment by plunging liquid jet (Cummins & Chanson, 1999), which is similar to what happens at the rear end of a Taylor bubble (Kockx et al., 2005); breaking of large waves (Dean & Stokes 2002) and processes at the front of a hydraulic jump (Chanson & Gualtieri, 2008; Xiang et al., 2014).The disturbance waves appearing in annular flow have much in common to hydraulic jumps, and one would expect them to be partially responsible for bubbles entrapment.

Comparing of our knowledge on wavy structure of disturbance waves and fast ripples (Cherdantsev et al., 2014) to the descriptions of bubbles entrapment process given by both Woodmansee & Hanratty (1969), "*ripples once lifted from the interface fall forward onto the liquid film*") and Rodriguez & Shedd (2004b), "*peaks or crests that entrap pockets of air when folding onto the bulk liquid*"), suggests that one more scenario of entrapment is related to the fast ripples falling onto the base film in front of a disturbance wave. A specific search for such events was performed throughout the whole amount of the data. Within the limitations of the present method it is difficult to confirm that overturning/falling of a fast ripple takes place, since only one value of apparent "film thickness", h, is obtained for each combination of x, y and t. Still, identification of such events was possible based on visual inspection of the data in graphical form. An example sequence of frames showing such an event is given in Fig. 7 with full video of this event shown in Video 3.

In Fig. 7(a) a fast ripple can be seen starting to overturn and partially "hang" above the base film. Its front edge, marked as (1), can be seen as a contrast in the brightness. In front of this line, h corresponds only to the base film thickness; in between the lines (1) and (2), h is produced by a combination of fluorescence inside both the base film and the fast ripple hanging above it. The bright line (2) appears due to total internal reflection of the laser light at the junction between the fast ripple and the base film, where the interface inevitably becomes vertical. An observation supporting this interpretation is linked to the bubbles (3) and (4) visible between the lines (1) and (2). The two bubbles marked by (3) came from the left inside the fast ripple; they are moving much faster than the one marked by (4), located inside the base film. This behaviour is clear at the beginning of Video 3.

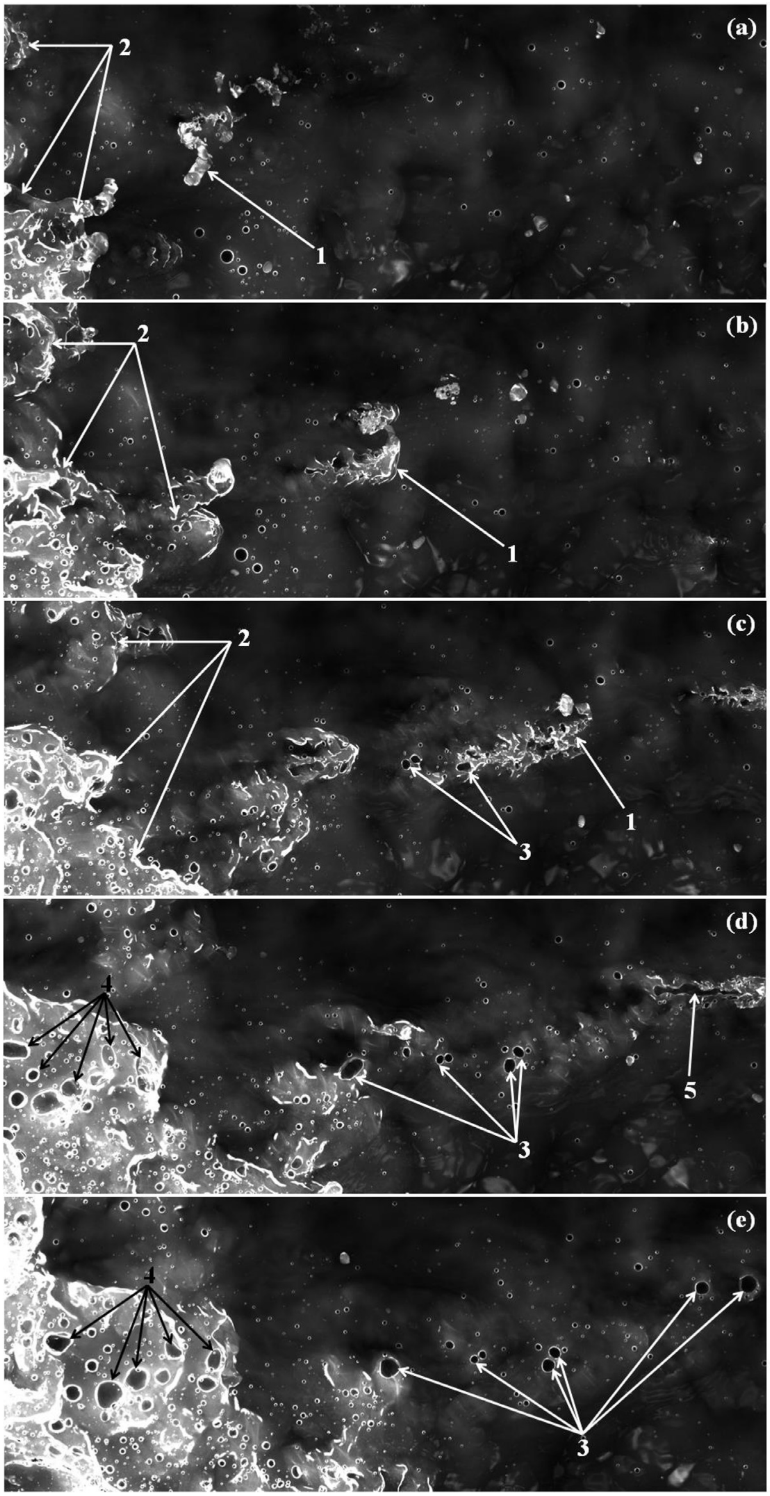

Fig. 6. Entrapment of bubbles due to oblique impact of remnants of a liquid bag onto the base film in front of a disturbance wave. The numbers denote: remnants of a liquid bag (1), front of disturbance wave (2), new entrapped bubbles (3), large bubbles inside the disturbance wave (4), ditch created by a lump of liquid protruding over film surface (5). $Re_L = 360$, $V_G = 30$ m/s. The full *RoI* (51 mm × 20 mm) is shown. The time increases downwards with the time step of 2 ms.

Later in time, the contact line (2) is being deformed, with its side edges moving faster than the front part (Fig. 7(b)). In this way, a three-dimensional pocket of air is formed with its front part still open. At the stages (c-d) the pocket is finally closed when the fast ripple's crest comes into contact with the base film. The side edges of the contact line (2) close to form the border of a new large bubble (Fig. 7(e)). Though the bubbles created this way can be large, this kind of event is relatively rare. It was mostly observed at the lowest gas velocities and the largest liquid flow rates. We assume this phenomenon is affected by neither shape nor the size of the duct if the duct's wetted perimeter is much larger than the typical transverse size of a fast ripple.

It is worth noticing that both bubbles marked as (3) survives that process, moving with high but variable speed and "outlive"

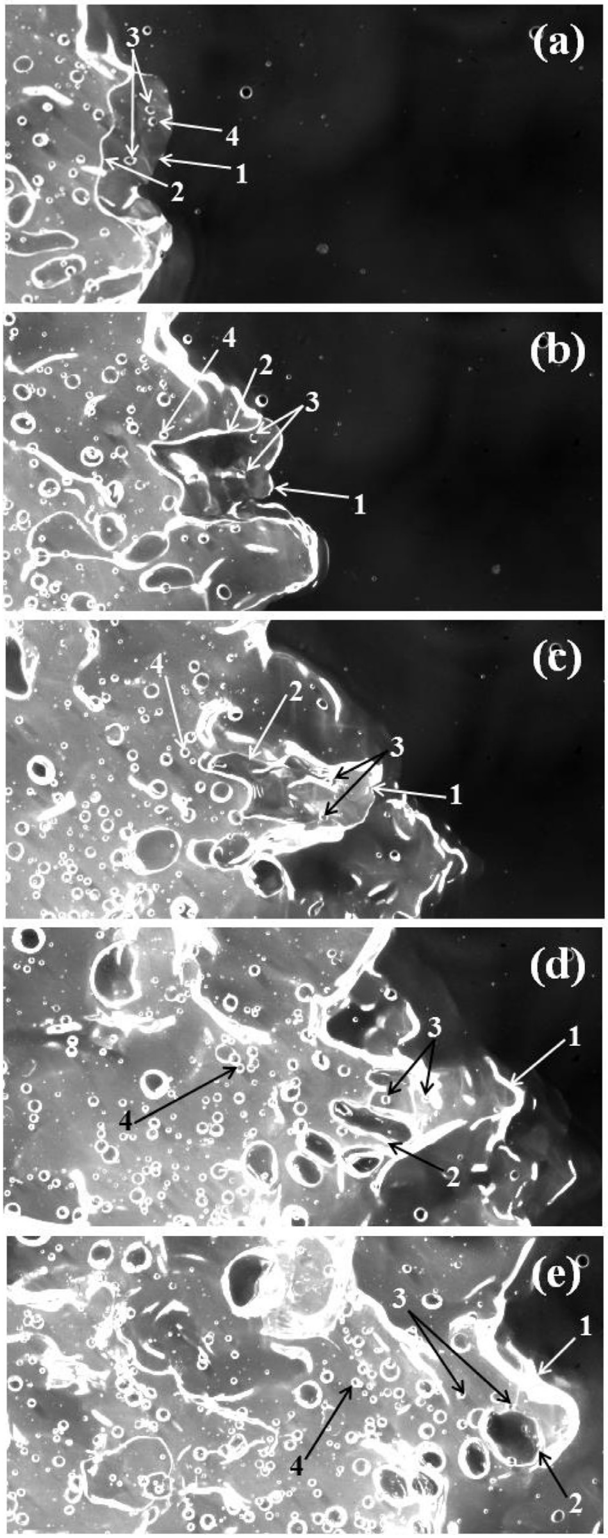

Fig. 7. Entrapment of a large bubble due to overturning of a fast ripple wave. $Re_L = 520$, $V_G = 25$ m/s. Image size is 19.2 mm by 9.6 mm. Relative time: 0 ms (a); 1.6 ms (b); 3.2 ms (c); 5.2 ms (d); 7.7 ms (e). The numbers denote: Front edge of the overturning ripple (1); the "contact line" between the overturning ripple and the base film (2); small bubbles inside the overturning ripple (3); a small bubble inside the base film (4).

the fast ripple that carried them. The bubble (4) flows under the disturbance wave as the wave overtakes it. Over a long time (from (a) to (c)) it does not shift significantly along the *x*-coordinate; but beginning from (d) it moves forward much more quickly. Possibly, it shifts along the vertical coordinate, *z*, and rises into the layer of liquid moving with a much higher speed. The detailed quantitative analysis of bubbles movement will be given in Section 5.

3.2. Collapse of bubbles

We have discussed the creation of bubbles using some of the many examples seen in the results taken. In the analysis of all the videos it was also noticed that some bubbles were unstable and collapsed. On the basis of our visual observations, we can conclude that the entrapped bubbles may collapse for two main reasons: either because of various external perturbations, or because it is trapped between the wall and the interface.

There are several sources of external perturbations able to cause the collapse of a bubble. These types of perturbations include:

- Either impact of a droplet or collapse of another bubble next to the bubble under consideration; in this case the bubble is being broken by the shock of either the expanding crater, protruding furrow or a circular wave produced by the collapsing bubble.
- When a bubble is inside a disturbance wave, it undergoes numerous changes in both longitudinal and transverse velocity together with shape deformations. These perturbations may be related to the movement of the fast ripples, which demonstrate large fluctuations in behaviour when travelling across the disturbance wave and interact with each other. Another possible reason of such behaviour of bubbles is their interaction to large-scale turbulent vortices which might exist inside the disturbance waves.
- A fraction of the new-created bubbles in a furrow region collapse promptly (see Section 3.3 in Cherdantsev et al., 2017). We suppose this happens due to strong shear beneath the interface, induced by the 'furrowing' droplet, and subsequent recovery flow.

At the same time, it is possible to observe the collapse of bubbles without any obvious external reason. Fig. 8 shows an example of a temporal sequence of frames showing such an event. Figures on the right show the apparent film thickness along the longitudinal cross-section of the images to the left. When the bubble collapses, the surrounding liquid flows into the space previously occupied by the bubble and forms a central jet that is similar to a jet appearing at the final stages of normal droplet impact (see Worthington, 1908). At the same time, a circular expanding wave is generated due to the collapse.

A search for bubbles collapsing without external perturbation has shown that such event is not very frequent: in total, about 120 events of this kind were detected during 5.4 s. During the search, only the bubbles which existed long enough prior to collapse were selected. Such bubbles appeared to be relatively large. As a rule, they have recently "escaped" a disturbance wave through its rear slope inside a newly-generated slow ripple. Prior to collapse, such bubbles start to slow down; this could be interpreted as sticking to the wall. In such a case, the ripple continues its movement and local film thickness around the bubble decreases as the ripple wave passes. Thus, the bubble becomes too large to survive in the trough between the ripples and collapses.

To characterise the process quantitatively, for each collapsing bubble its equivalent diameter, *D* (see Section 2.3), residual film thickness, h_R, and encompassing film thickness, h_E, (see Section 2.4) were obtained. The measurement results are shown in Fig. 9(a) in form of histograms. It can be seen that bubble diameter in *x*-*y* plane, *D*, is generally larger than the film thickness,

Please cite this article as: D.B. Hann et al., Study of bubbles entrapped into a gas-sheared liquid film, International Journal of Multiphase Flow (2018), https://doi.org/10.1016/j.ijmultiphaseflow.2018.07.001

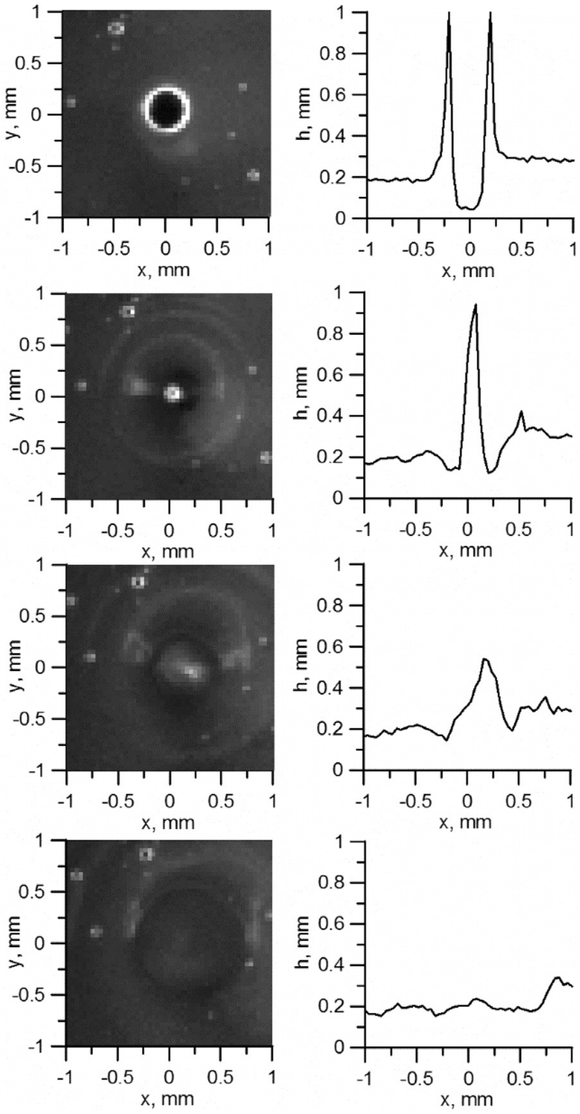

Fig. 8. Sequence of frames (time step is 0.2 ms) showing the collapse of a bubble. Images on the left show graphical representation of film thickness in the vicinity of the bubble. Images on the right show apparent film thickness profiles along the line $y = 0$. $Re_L = 360$, $V_G = 30$ m/s.

encompassing the bubble, h_E. The residual film thickness around the ready-to-collapse bubbles is thin: its median value is less than 40 µm.

Since the residual film thickness is small, comparing the bubble's size in *x*-*y* plane and thickness of liquid film encompassing the bubble for individual bubbles can provide us with a general idea on possible three-dimensional shape of the bubbles and the conditions of a bubble's existence. Such a comparison for the bubbles prior to collapse is shown in Fig. 9(b). The majority of bubbles collapse in the region $D/2 < h_E < D$. This relationship does not necessarily mean that a bubble is "squashed" up to two times along *z*-coordinate between the wall and the film surface. Alternatively, the top part of a bubble may rise above the surface of surrounding liquid, being up to two times higher.

The same comparison of D vs h_E for all the detected bubbles (not only the collapsing ones) for one combination of gas and liquid flow rates is presented in Fig. 10 in form of a two-dimensional histogram.

For visualisation purposes, the local brightness of each two-dimensional bin in Fig. 10 is proportional to square root of the number of bubbles belonging to the particular narrow ranges of D **and** h_E. The majority of existing bubbles belongs to the region $h_E > D$ and nearly no bubbles are detected in the region $h_E < D/2$. In the intermediate region a relatively small number of bubbles exists. It is expected that these bubbles are short-lived due to high probability of collapse.

3.3. Summary of bubble generation and creation

We have shown samples of three different entrainment mechanisms noted in the extensive sequences of video obtained in this analysis. From the observation of the records it is possible to see that bubbles are constantly being created and destroyed. To understand how the fluid and gas properties affect the ratio of creation and destruction processes, it is necessary to make a count of the size and concentration of the bubbles. This is carried out in the next section.

4. Size and concentration of entrapped bubbles

As a result of the application of the algorithm of automatic detection and processing of bubbles, described in Section 2.3, the properties of the bubbles can be studied quantitatively with relation to flow rates of both phases and also with respect to presence or absence of disturbance waves.

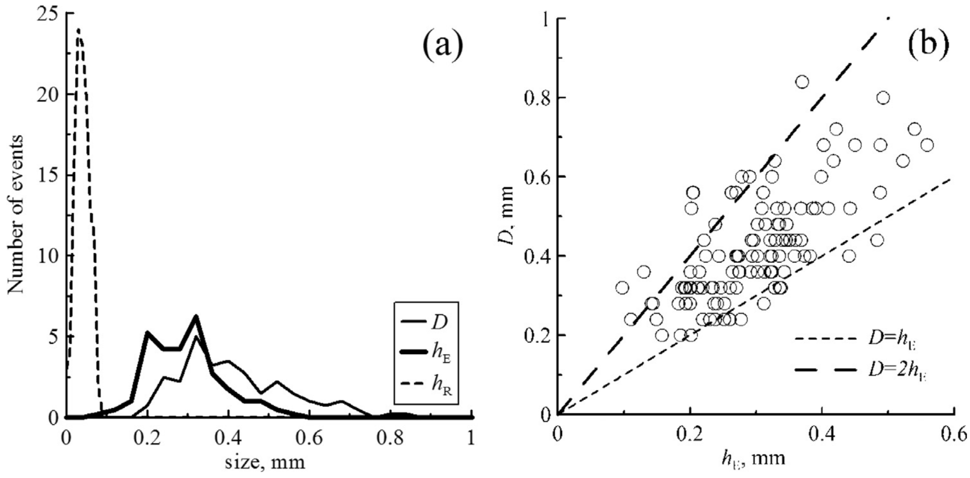

Fig. 9. Analysis of bubbles on the verge of collapsing. a) Distributions of bubble diameter in *x*-*y* plane, D, thickness of film encompassing the bubble, h_E, and thickness of residual film around the bubble, h_R. b) Comparison of bubble diameter in *x*-*y* plane *vs* thickness of liquid film encompassing the bubble for all bubbles individually.

Please cite this article as: D.B. Hann et al., Study of bubbles entrapped into a gas-sheared liquid film, International Journal of Multiphase Flow (2018), https://doi.org/10.1016/j.ijmultiphaseflow.2018.07.001

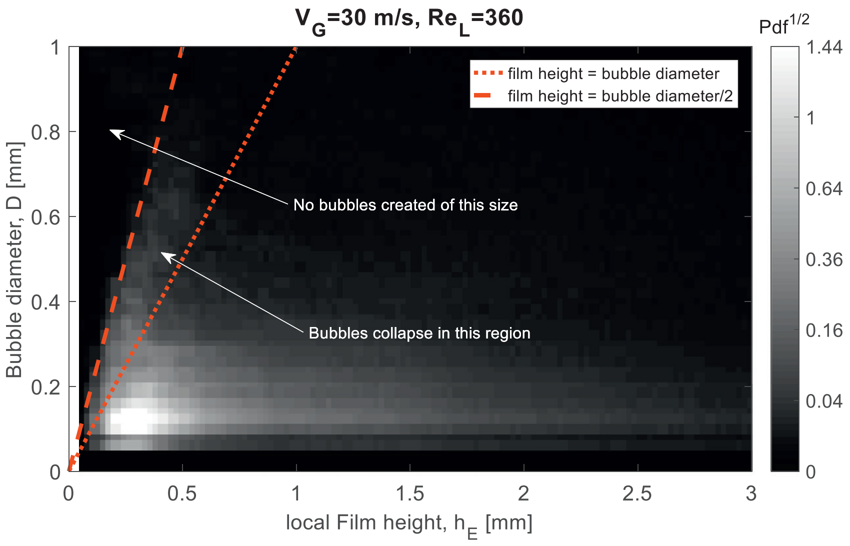

Fig. 10. Joint probability between the bubble diameter in *x-y* plane and the thickness of the encompassing film for one combination of flow rates. Construction lines are $D = h_E$ and $D = 2h_E$.

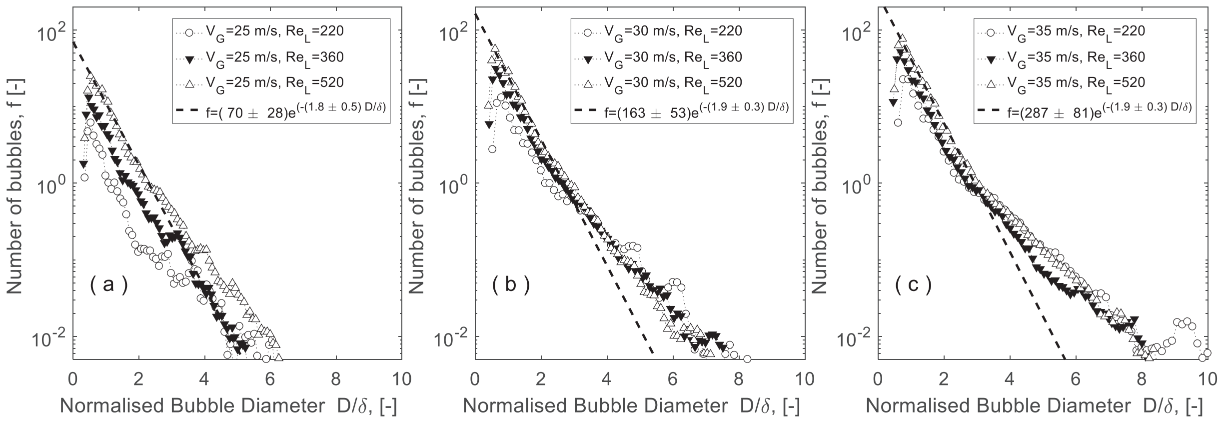

Fig. 11. The distributions of bubbles by size normalised by base film thickness, δ, for $V_G = 25$ m/s (a), $V_G = 30$ m/s (b) and $V_G = 35$ m/s (c).The bin size is 40 µm. An exponential fit is made over the same region as Rodriguez & Shedd (2004a). The 95% confidence level of the curve fit to $Re_L = 520$ is given in the fitted equations.

4.1. Bubble sizes, concentrations and relation to creation mechanisms

The size distributions of the bubbles can be seen in Fig. 11. The total number of identified bubbles was normalised by the number of frames in the record, thus giving the number of bubbles per image. This quantity increases with gas velocity, and, by a lesser degree, with liquid Reynolds number. To facilitate the comparison to the results of Rodriguez & Shedd (2004a), the ordinate axis is given in logarithmic scale and the abscissa axis is normalised by the base film thickness, δ. The latter was defined as the modal value of the film thickness distribution.The bin width of the distributions prior to normalisation by δ is equal to 40 µm.

Rodriguez & Shedd (2004a) studied the bubbles in the base film only and the parameter D/δ did not exceed 1.5 in their plots compared to our range up to 10. In the low diameter region, the distributions were found to be of exponential form $f = N\exp(-bD/\delta)$. This form is also true for our distributions within that range of D/δ values, except for the smallest bubbles ($D \le 0.12$ mm), where a slope of the opposite sign can be observed, possibly due to the difficulty of measuring the smallest size of bubbles. Rodriguez & Shedd (2004a) reported a similar behaviour in their preliminary low-resolution experiments but this disappeared after the spatial resolution was improved. The spatial resolution of the present measurement system is about 10 times worse than that of Rodriguez & Shedd (2004a), so the considerations above are applicable to the present case as well. As mentioned in Sections 2.3 and 2.4, the bubbles smaller than two pixels in size ($D \le 0.08$ mm) are nearly impossible to be detected by the algorithm, which greatly reduces their frequency and creates this inverse slope of the distribution. Moreover, some of slightly larger bubbles ($0.08\,\text{mm} \le D \le 0.16$ mm) may also be missed due to noise or low contrast. In such a case, the probability of a bubble's detection grows with the bubbles size, approaching unity around $D = 0.2$ mm. The latter may lead to change of slope of the decaying part of the distribution in the range $0.12\,\text{mm} < D < 0.2$ mm.

The exponential decrements were estimated for each regime point within a limited range of D/δ where monotonic linear decay was observed. The approximation is shown by the dashed red line for $Re_L = 520$ for each value of V_G in Fig. 11 and summarised for all cases in Fig 12.These decrements were found to be the same (about 1.9) for all flow conditions within the 95% uncertainty bounds. This value is about 2–3 times smaller than those obtained by Rodriguez & Shedd (2004a) for similar gas velocities. This discrepancy might be attributed to the lack of spatial resolution in the present experiments as described above. Besides, Rodriguez & Shedd (2004a) conducted their experiments at much larger down-

Please cite this article as: D.B. Hann et al., Study of bubbles entrapped into a gas-sheared liquid film, International Journal of Multiphase Flow (2018), https://doi.org/10.1016/j.ijmultiphaseflow.2018.07.001

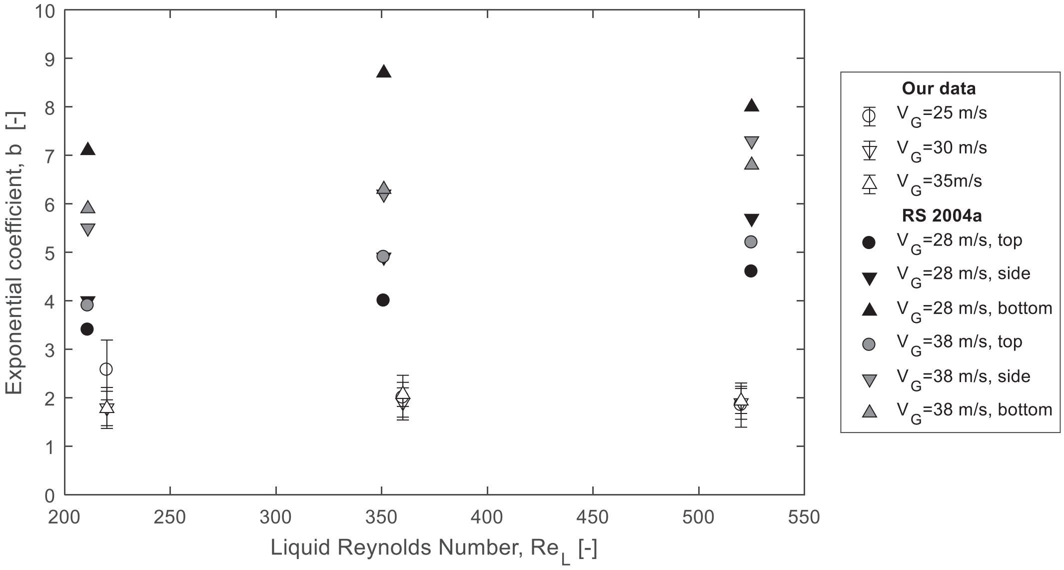

Fig. 12. The exponent *b* from the exponential fit (see Fig. 11) for all 9 cases studied here. Error bars are 95% confidence levels of curve fit. Data from Rodriguez & Shedd (2004a) is shown for comparison.

stream distances. The increasing downstream distance may also affect the shape of the distribution, since the smaller bubbles are expected to be more durable to collapse on the reasons described in Section 3.2.

Rodriguez & Shedd (2004a) explain the exponential shape of the distribution by the cascade of break-up of larger bubbles to form smaller ones. However, the events of bubbles break-up are extremely rare and they may occur only when a very large bubble (over 1 mm) is entrapped inside a disturbance wave due to the scenario described in Section 3.1.3. Such a bubble may split into two bubbles, but there is no further cascade of break-up events. In a severe situation, bubbles of small and medium size would rather collapse completely than split into smaller ones. Thus, we should emphasise that the number of smaller bubbles is higher not due to the bubbles break-up, but due to higher probability of small bubbles both to be created (see Section 3.1.1) and to survive in the base film (see Section 3.2).

The present distributions extend to larger bubbles sizes than those from Rodriguez & Shedd (2004a) due to the taking into account larger bubbles trapped inside the disturbance waves. It can be noted in Fig. 11 that there is a change in slope above a certain value of D/δ which is larger than that measured by Rodriguez & Shedd (2004a). This transition occurs at increasing values of D/δ as the gas velocity is increased, but does not appear to have much dependence on Re_L.

In order to investigate the effect of disturbance waves on bubbles concentration and sizes, temporal records of film thickness averaged over the whole *RoI*, were constructed. For comparison, the longitudinal size of a disturbance wave (about 3–4 cm in our conditions) is slightly shorter than that of *RoI*. Nonetheless, the presence of a disturbance wave yields a well-pronounced hump in a temporal record of spatially averaged film thickness (see Fig. 13). This is a simple way to detect presence of a disturbance wave in the *RoI* and relate it to the characteristics of the bubbles. In Fig. 13 the temporal record of volume of fluid in the *RoI* (i.e., spatially averaged film thickness multiplied by the area of *RoI*) is superimposed onto the temporal record of the number of bubbles inside *RoI*. An obvious strong correlation between the two records confirms the previously mentioned qualitative observation on an increased number of bubbles inside the disturbance waves.

It is also interesting to compare the shape of the instantaneous distributions of bubble size inside and outside the disturbance waves. These correspond to a time when there is a disturbance wave (e.g., time instant t_1 in Fig. 13) and to a time when there is no disturbance wave (e.g., time instant t_2). The noise level in individual distributions is quite high, so to understand the effect that the disturbance wave has on the bubble size and velocity distributions, a POD filter was used to identify the 2 modes (representing the main states of the flow, i.e. with and without disturbance waves) which contain 95% of the energy of the distribution and the distributions were reconstructed only using these two modal shapes that represent the two most probable modes (see Hann et al., 2015 for more complete explanation of POD technique). To increase comprehensiveness of the visual comparison, the distributions were normalised along the ordinate axis by the total number of bubbles in the *RoI*. Fig. 14 shows an example of such a comparison for the two time instants identified in Fig. 13.

The normalised distributions are almost identical within the range of $D < 0.5$ mm. This similarity suggests that the small bubbles inside the base film and inside disturbance waves are of the same origin. Namely, the small bubbles are created due to oblique impacts of droplets depositing from the gas core with furrow formation (as described in Section 3.1.1). These bubbles travel inside the base film until a disturbance wave overtakes them. When a disturbance wave passes above those bubbles there is a chance that a bubble would be captured by the disturbance wave and travel inside it with high speed, as it was observed for the bubble (4) in Fig. 7. Thus, disturbance waves "collect" numerous small bubbles from the base film. This behaviour explains the difference in bubbles number shown in Fig. 13.

The main difference between the two distributions is observed in the range of large diameters ($D > 0.5$ mm) and consists in a noticeably higher probability of large bubbles inside the disturbance waves. There are two reasons for this difference. Firstly, the large bubbles are mostly created by a different mechanism: impact of large-scale liquid lumps remaining from former liquid bags/ligaments (see Section 3.1.2) and overturning of the fast ripples (Section 3.1.3). Both mechanisms occur in front of the disturbance waves and the new bubbles are promptly overtaken by the disturbance waves. Secondly (as shown in Section 3.2) the large bubbles are likely to collapse inside the thin base film which is

Please cite this article as: D.B. Hann et al., Study of bubbles entrapped into a gas-sheared liquid film, International Journal of Multiphase Flow (2018), https://doi.org/10.1016/j.ijmultiphaseflow.2018.07.001

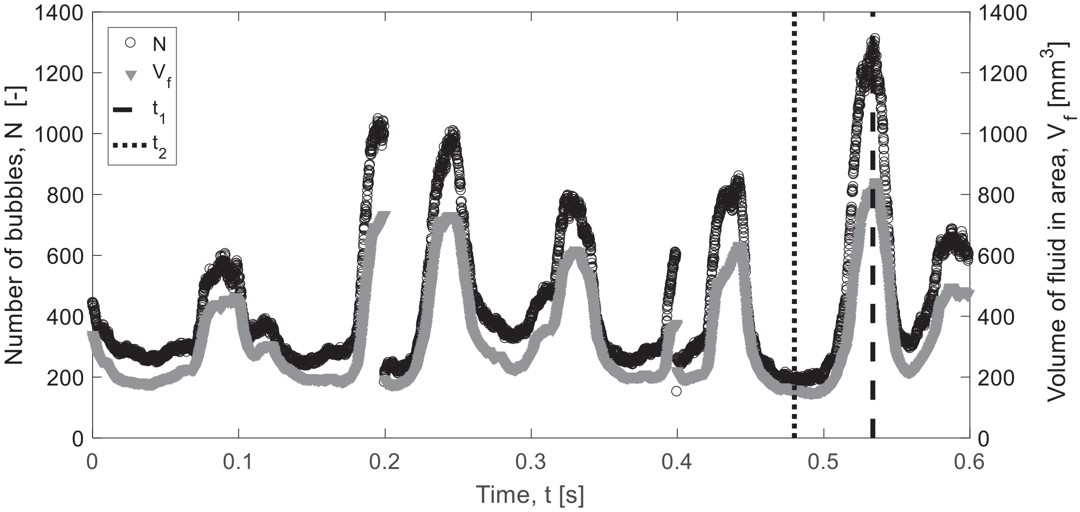

Fig. 13. Temporal records of the number of bubbles present in each frame, *N*, and volume of liquid contained inside RoI, V_f, in each frame. Peaks are associated with the presence of a disturbance wave. The sharp discontinuities are due to this being three 0.2 s segments stitched together. The flow conditions are V_G= 35 m/s and Re_L= 520. $\boldsymbol{t}_1$ and $\boldsymbol{t}_2$ are noted as respectively; the time of a disturbance wave, and of the base film passing the measurement area.

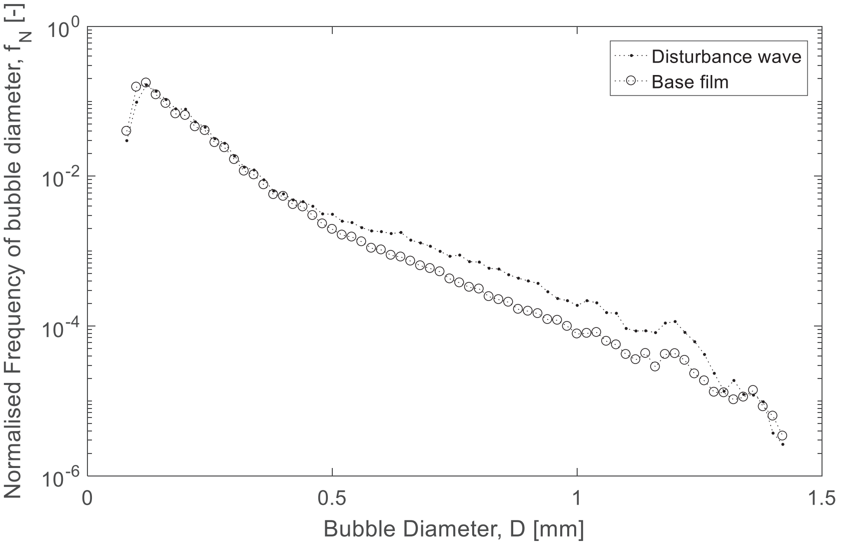

Fig. 14. The bubble size distributions at times t_1 and t_2 (see Fig. 13) corresponding to the location of a disturbance wave and base film, respectively. Flow parameters are the same as in Fig. 13.

about 0.2 mm for the flow regime shown in Fig. 14. Thus, even if a large bubble manages to escape from the disturbance wave through its rear end, it will eventually collapse due to being trapped inside thin base film in a trough between the slow ripples.

4.2. Understanding bubble density

The strong correlation that exists between the number of bubbles and the volume of film liquid as previously shown in Fig. 13, suggests that there is a direct relationship between the two. To investigate this relationship, these two parameters were directly compared against each other for each frame and this is shown in Fig. 15 for all combinations of gas and liquid flow rates. It could be noticed that increase of both the liquid volume and the number of bubbles occurs in loops showing a slight hysteresis between the two quantities. Every loop is created in a clockwise direction, which denotes that the number of bubbles is slightly higher in front of a disturbance wave than in the rear of it. For simplicity, the dependency of the number of bubbles on volume of fluid for each flow regime can be approximated as a linear one. The 95% confidence level of the linear fit is determined to be very small (<3%). The slope of each line characterises the number of bubbles per unit liquid volume, or volumetric density of bubbles. This quantity is a function of both V_G and Re_L.

The measured bubble density is plotted in Fig. 16 against V_G and Re_L. Dependencies of both kinds can be fitted as

$$N/V_f = A(V_G - V_{G0})^{0.5},\ N/V_f = B(Re_L - Re_{L0})^{0.5},$$

where V_{G0} varies with the liquid Reynolds number and Re_{L0} varies with gas velocity. The density of bubbles increases with both liquid and gas flow rates, which could be expected since the rate of liquid entrainment and, hence, the number of depositing droplets creating small bubbles in the base film also grows with both parameters. The estimated square root dependence suggests that the bubble densities are saturated at larger flow rates of liquid and gas. It was noted in Section 3.2 that the impact of a droplet on the film could burst bubbles. Thus, when the base film is uniformly seeded with bubbles with high enough concentration, new furrow impact would not only create new bubbles, but also destroy old ones, thus limiting the number of bubbles possible in the film.

Please cite this article as: D.B. Hann et al., Study of bubbles entrapped into a gas-sheared liquid film, International Journal of Multiphase Flow (2018), https://doi.org/10.1016/j.ijmultiphaseflow.2018.07.001

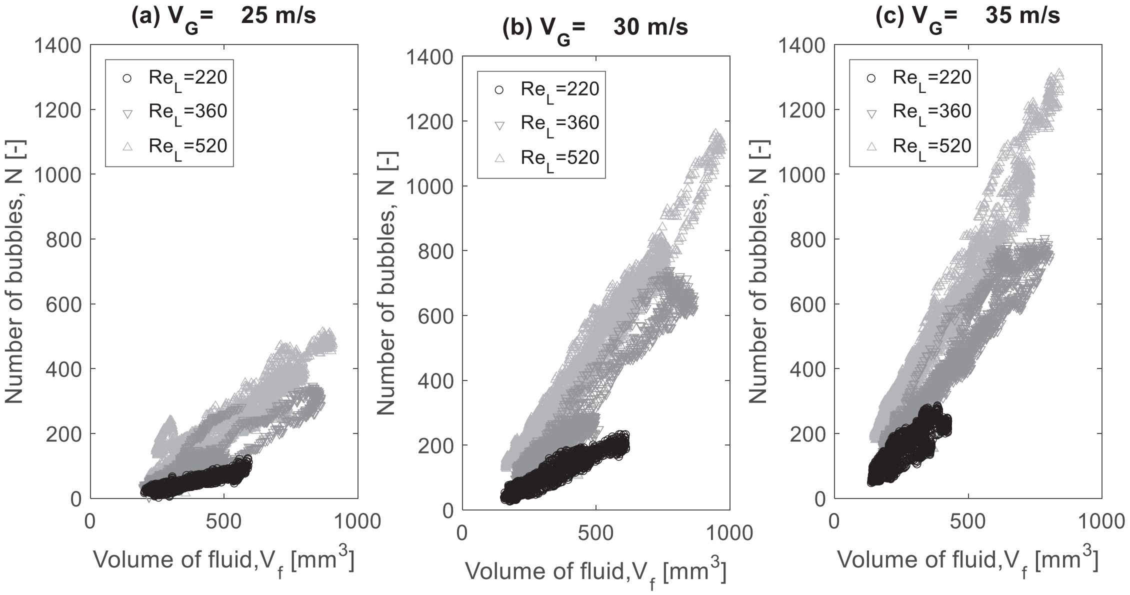

Fig. 15. The relationship between the number of bubbles and the total volume of liquid present in each frame.

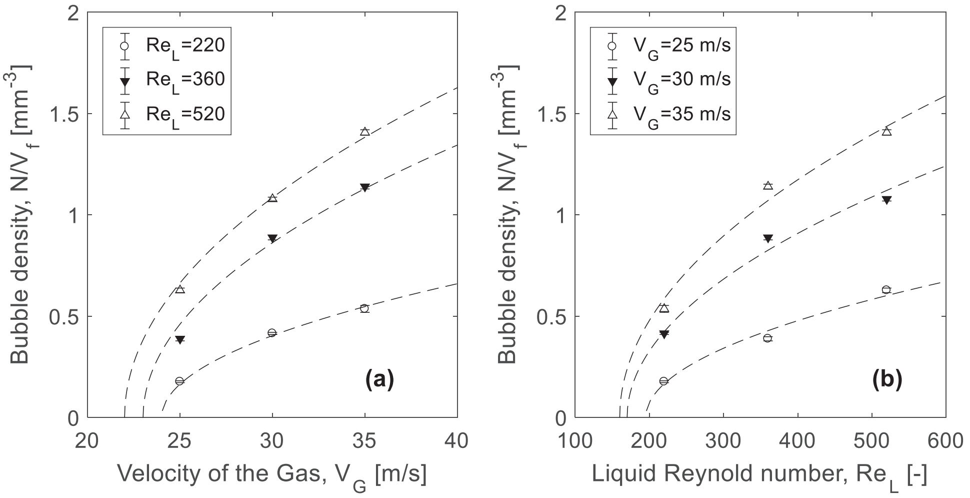

Fig. 16. Dependence of bubbles density on gas velocity (a) and liquid Reynolds number (b). Error bars are 95% uncertainty in the linear gradients of the dependencies in Fig 15.

The above dependencies give us six pairs of points: three points with $\{V_{G0}, Re_L\}$ and three points $\{V_G, Re_{L0}\}$. These points, which we suppose to mark the transition to bubbles entrapment, are shown in Fig. 17. The obtained line is of similar shape as the transitions to disturbance waves and liquid entrainment given by Woodmansee & Hanratty (1969) who used duct of the same orientation, shape and height and different only in width. Indeed, two of three mechanisms of bubbles creation described in Section 3.1 require the presence of liquid entrainment. The third one requires the presence of disturbance waves generating overturning fast ripples. Nonetheless, the "transition to bubbles" occurs at higher gas velocities than the "transition to droplets". This quantitative difference is expected since the above considerations on bubbles volumetric density are extrapolated from the conditions when the bubbles are distributed in a relatively uniform fashion in *x*-*y* plane and not as single patches appearing due to impacts of single droplets. Besides, the probabilities of creation and deposition of droplets are related to the downstream distance and the latter was much longer in Woodmansee & Hanratty (1969) experiments.

Combining the dependencies of the number of bubbles on volume of liquid (Fig. 15) with the data on bubbles size, the volume of entrapped air dependency on volume of liquid in the image can be analysed. This analysis is necessary since the size of the bubbles can be seen to decrease as the gas velocity is increased. The volume of entrapped air also linearly grows with the volume of liquid. The gradient of the straight line characterises the degree of aeration of liquid film, which is shown in Fig. 18(a). An increase in Re_L will cause a non-linear increase in aeration, which is to be expected since increasing Re_L will increase the number and the volume of disturbance waves. It should be noted that both the amplitude and frequency of disturbance waves grow with Re_L in non-linear manner, becoming less sensitive to increase in Re_L at large values of Re_L. A similar behaviour to this growth of disturbance waves with Re_L is observed in Fig. 18(a). It appears that increasing the velocity of the gas produces an increase in aeration, which appears to be stabilising at the higher gas velocity. Fig. 18(b) shows the Sauter mean diameter of the bubbles, which is only weakly dependent on Re_L, but decreases significantly as the gas velocity is increased. Since the liquid film becomes thinner due to stronger

Please cite this article as: D.B. Hann et al., Study of bubbles entrapped into a gas-sheared liquid film, International Journal of Multiphase Flow (2018), https://doi.org/10.1016/j.ijmultiphaseflow.2018.07.001

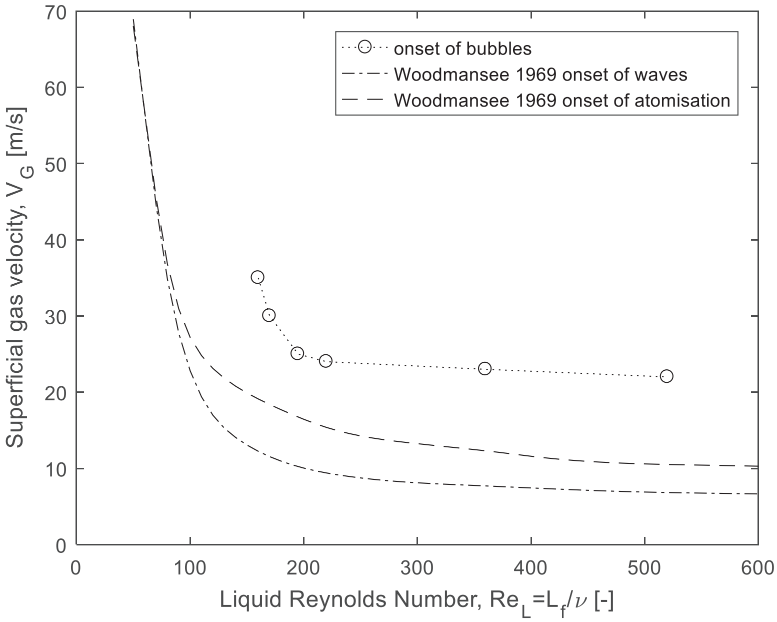

Fig. 17. Comparison of the zero crossing values from Fig. 16 to the transition to disturbance waves and entrainment by Woodmansee & Hanratty (1969).

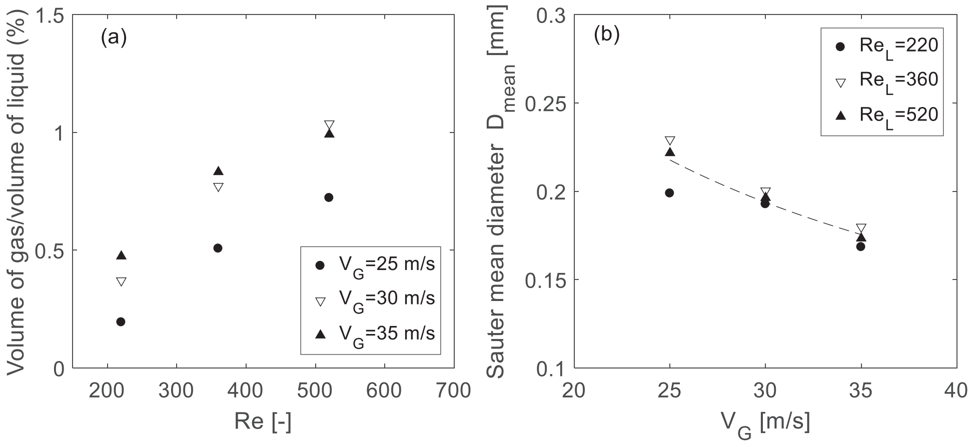

Fig. 18. (a) Effect of Liquid Reynolds number on the liquid film aeration and (b) Effect of gas velocity on the Sauter mean diameter of the bubbles.

gas shear, smaller bubbles are more likely to survive in these films. This decrease in bubbles volume correlates to the growth of bubbles number with gas velocity and may thus explain the saturation of the aeration with V_G shown in Fig. 18(a).

5. Analysis of bubble velocity

As shown in the previous section, the number and size of bubbles are larger in the disturbance waves than in the base film. In this section the speeds of the individual bubbles are analysed and used in combination with the encompassing film thickness to provide insight into the velocity profile inside liquid film.

5.1. Distribution of bubble velocity

The bubble velocity distributions are more complex than the bubble size distributions. The flow situation present is not stationary, but consists of two cases related to the intermittent nature of the flow; fast-moving disturbance waves and slow-moving base film. As a result, the distributions in general have two potential values (see Fig. 19), which would be hypothesised from the premise that faster bubbles are in the disturbance waves and the slower bubbles are in the base film between the waves.

This idea can be verified by considering the temporal evolution of instantaneous distribution of the bubble velocity. An example of such evolution is shown in Fig. 20 for the same flow regime as in Fig. 13. Each column of Fig. 20 is a graphical representation of an instantaneous distribution of bubble velocity, with brightness of the image directly proportional to the number of bubbles in a bin with width 0.1 m/s. As a disturbance wave enters the *RoI*, the whole distribution is shifted towards larger values and spread over wider range of velocities. Comparison is shown in Fig. 21 for the same time instants, t_1 and t_2, corresponding to a disturbance wave and base film, respectively. The bubbles in the base film move with modal velocity of 0.4 m/s; the range of velocities is limited by about 1 m/s. Inside the disturbance wave, the modal velocity value is 1.5 m/s; still, the values close to zero exist in the distribution. The velocity variation - defined as standard deviation normalised by the mean value - is approximately the same for both base film and disturbance waves.

Visual examination of spatiotemporal trajectories of bubbles in the base film has been performed using the *x*-*t* representation of the BBLIF film thickness data (see, e.g., Cherdantsev et al., 2014).

Please cite this article as: D.B. Hann et al., Study of bubbles entrapped into a gas-sheared liquid film, International Journal of Multiphase Flow (2018), https://doi.org/10.1016/j.ijmultiphaseflow.2018.07.001

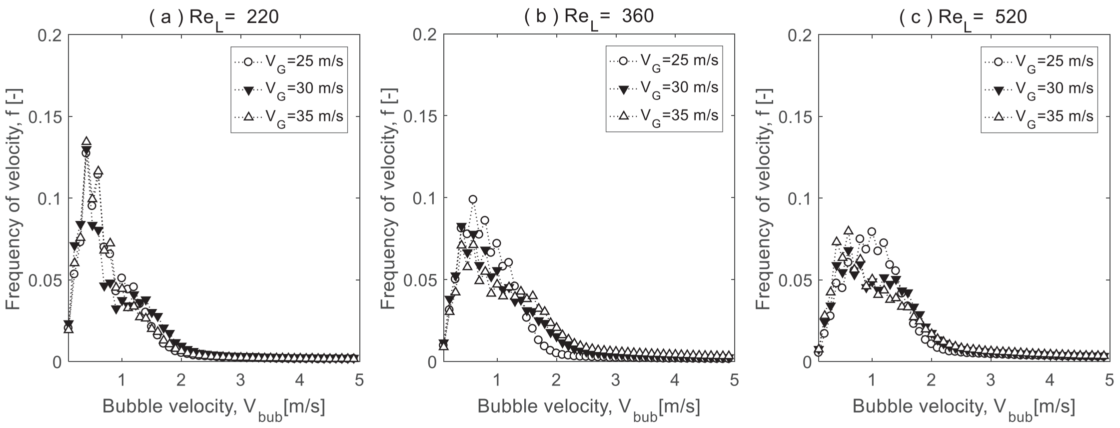

Fig. 19. Comparison of bubble velocity distributions for $Re_L = 220$ (a), $Re_L = 360$ (b) and $Re_L = 520$ (c).

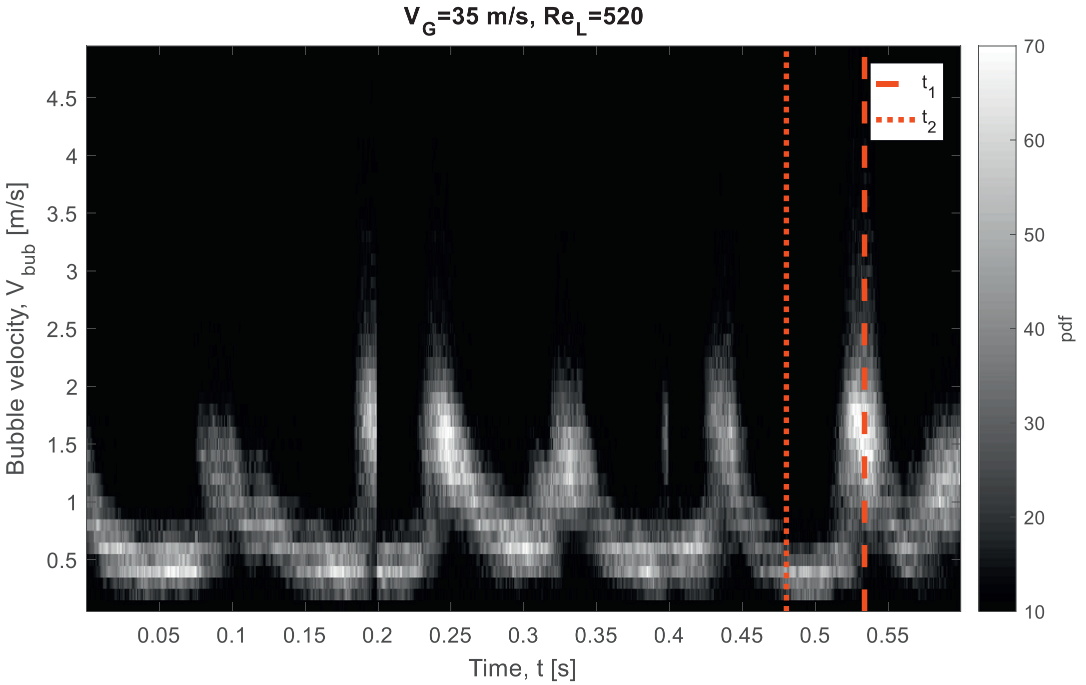

Fig. 20. Time sequence showing the probability of particular bubble velocities with time. Note that this is the stitching of 3 segments so there are discontinuities at 0.2 and 0.4 s. Identified are the same locations as for Fig. 13 showing location of the disturbance wave, t_1, and the base film between the disturbance waves, t_2.

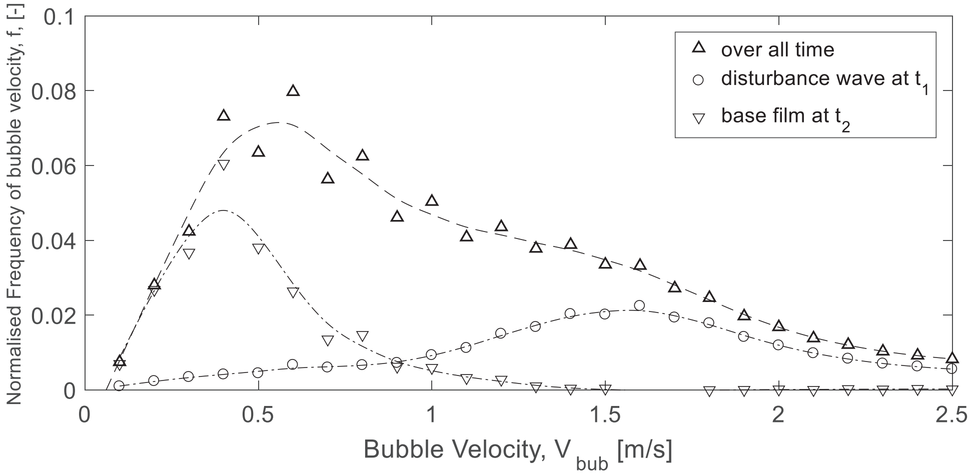

Fig. 21. Comparison of the velocity distribution in the disturbance wave (t_1) and the base film (t_2) taken from Fig. 20.The shape of the complete velocity distribution is included for comparison. Component distributions are divided by 4 to put them on the same scale.

Please cite this article as: D.B. Hann et al., Study of bubbles entrapped into a gas-sheared liquid film, International Journal of Multiphase Flow (2018), https://doi.org/10.1016/j.ijmultiphaseflow.2018.07.001

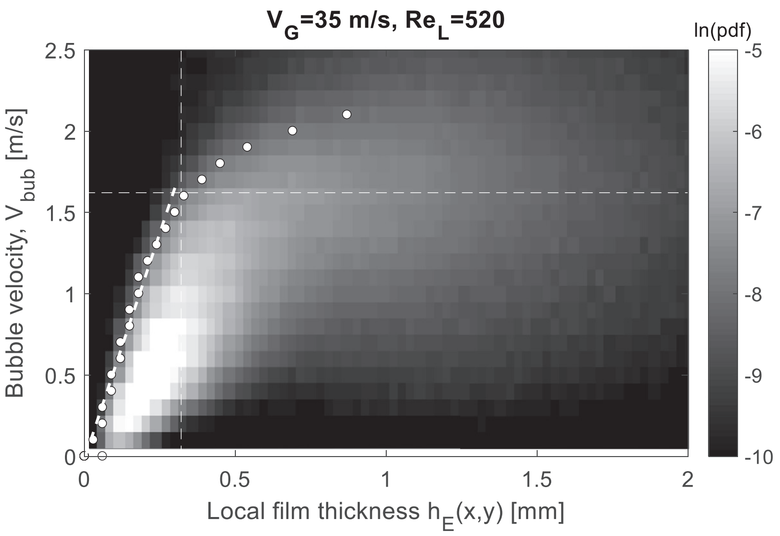

Fig. 22. Probability function comparing the bubble velocity against the local film thickness surrounding the bubble. Horizontal and vertical dashed lines show the average film thickness and average film velocity, respectively. The fastest bubbles for each film thicknesses are identified and the gradient of this line for thin films is measured.

When such a bubble is overtaken by a slow ripple, it was seen to accelerate toward the velocity of the ripple. Due to the small velocity difference, it eventually escapes the slow ripple through its rear end and its velocity decreases back about two times. This observation in combination with the effect of disturbance waves shown in Fig. 20 suggests that the bubbles tend to follow the flow of surrounding liquid.

5.2. Studying liquid film velocity profile using bubbles as tracers

Indeed, it should be expected that the bubbles of observed range of size would follow the liquid flow at relatively low velocity. Upper estimation of Stokes number (1-mm bubble inside liquid flowing with speed of 2 m/s) gives the value of 0.133; the most probable values of bubble size and liquid velocity yield Stokes number one order of magnitude smaller inside disturbance waves and about two orders of magnitude smaller inside the base film. Besides, for the largest bubbles in the fastest liquid the bubble's Reynolds number can be high enough (of order of one thousand). Taking the effect of high Reynolds numbers would reduce Stokes number even further (see, e.g., Israel & Rosner, 1982). Thus, the bubbles can act as tracers. This conclusion is in agreement with analysis performed by Kopplin (2004).

The data on velocity profile inside liquid film in annular flow are relatively scarce. The most comprehensive studies of this kind were performed recently by Zadrazil & Markides (2014), who used PIV/PTV in downward flow and by Ashwood et al. (2015), who used micro-PIV in upward flow. In both cases tiny solid particles were used as tracers. In both cases, the time-averaged profile of longitudinal velocity component, $U_x(z)$, was obtained by averaging all measured values of U_x at certain value of z, without discriminating between the base film and the disturbance waves. The obtained profiles qualitatively resembled the so-called Universal Velocity Profile (UVP), derived from von Karman's single-phase turbulent boundary layer and consisting of linear wall layer and two logarithmic layers, namely, "buffer" and "turbulent" layers, see Ashwood et al. (2015) for details.

In contrast to these studies, there is no direct indication of the distance between the "tracer" and the wall in the present experiments. So, no direct measurement of velocity profile is possible. On the other hand, thickness of liquid film encompassing each bubble, h_E, is known, in contrast to the approach used by Kopplin (2004). Thus, some conclusions on the velocity profile can be made based on the present data, under an assumption that the longitudinal component of local liquid velocity, U_x, monotonically increases with distance from the wall, z. In such a case, all velocity values of bubbles belonging to a narrow range of h_E, characterise local velocities of liquid at the distances from the wall from 0 to h_E, and the maximum value from this sample shows $U_x(z = h_E)$. The assumption above is not necessarily true for an instantaneous velocity profile due to possible presence of various recirculation zones inside the film, see Zadrazil & Markides (2014). Nonetheless, we expect it to be correct for the velocity profile obtained by averaging over large number of instantaneous profiles.

Fig. 22 shows 2D-histogram of velocity and local film height, h_E, for individual bubbles. For comparison, the mean film height (δ_m) measured in this work, and the mean film velocity calculated from $U_m = L_f/\delta_m$ are shown on the distribution. The mean liquid velocity corresponds well to the mean velocity of the bubbles inside the disturbance waves, which supports the idea that the disturbance waves carry the major fraction of liquid (e.g., Han et al., 2006).

For each value of h_E, maximum value of bubbles velocity, U_{max}, can be identified as the velocity value higher than that of 98.5% of the bubbles entrapped by the film of the same thickness. The values of U_{max} are marked by the white dots in Fig. 22. At low h_E, U_{max} grows linearly with distance from the wall and so the gradient can be approximated by $U_{max}(h_E)/h_E$. This range thus indicates the thickness of "laminar" sub-layer at the wall in which shear flow defined by the wall shear stress is observed. Further from the wall, the dependence of U_{max} on h_E turns into a logarithmic one, as the Universal Velocity Profile would suggest. In order to quantitatively analyse the velocity profile obtained in form of $U_{max}(h_E)$, its gradient near the wall region was measured to determine an equivalent wall shear stress, τ_w, and this was used to convert the data for all gas and liquid flow rates into law of the wall units, U^+ and z^+.

The wall shear stress is here defined as:

$$\tau_w = \mu \left. \frac{U_{max}}{h_E} \right|_{h_E=0}$$

This can be used to estimate the friction velocity $U_\tau = \sqrt{\frac{\tau_w}{\rho_L}}$, which can be used to normalise the velocity and distance in the

Please cite this article as: D.B. Hann et al., Study of bubbles entrapped into a gas-sheared liquid film, International Journal of Multiphase Flow (2018), https://doi.org/10.1016/j.ijmultiphaseflow.2018.07.001

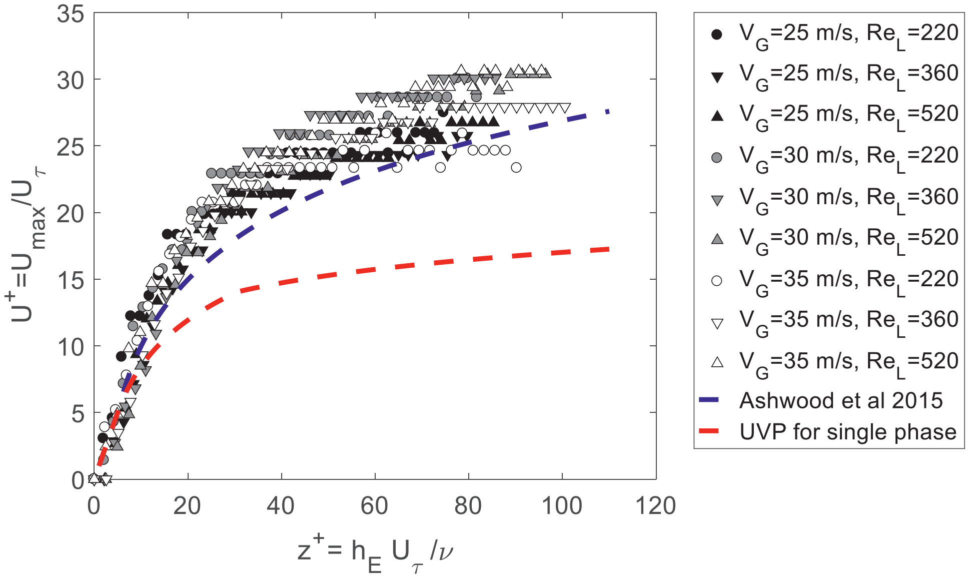

Fig. 23. Maximum velocity of the bubbles for different local film heights normalised using the equivalent wall shear stress to obtain law of wall units.

Universal Velocity Profile.

$$U^+ = \frac{U_{\max}}{U_\tau},\ z^+ = \frac{h_E U_\tau}{\nu}$$

Fig. 23 shows that for all cases there is a strong similarity in this normalised profile for all experimental conditions. At low h_E the flow has a linear, quasi-laminar profile, clearly shown up until about $z^+ = 10$. Above this value, the profile develops into a log-law region, but the U^+ values lie well above the UVP prediction, shown by the red line in Fig. 23. Similar disagreement was also observed by Ashwood et al. (2015) who have found that all UVP constants describing the velocity profile in both buffer and turbulent layers should be altered to fit their data. The velocity profile obtained in the present work is closer to that of Ashwood et al. (2015) than to UVP for single phase fluids. By re-analysing the results of Ashwood et al. (2015) and a large set of literature data on average film thickness, Cioncolini et al. (2015) concluded that both laminar and buffer layers may be thicker in annular flow conditions than those in single-phase flow, shifting the borders from $z^+ = 5$ and $z^+ = 30$ to $z^+ = 9$ and $z^+ = 40$, respectively.

The discrepancy between different sets of the results might be related to the aforementioned mixing-up of the two zones, namely, base film and disturbance waves. In the framework of such an approach, it is implicitly assumed that U_x should be dependent only on z, irrespectively to presence or absence of a disturbance wave at given x value. At the same time, the velocity profile in the two cases may be significantly different. This latter point is supported by measurements of instantaneous wall shear stress (see, e.g., Miya et al., 1971). Thus, significant uncertainty may arise from the different relationships between wall shear stress in different zones and also the variation in the intermittency of the disturbance waves with flow conditions.

In our case, the linear and logarithmic parts of velocity profiles were actually obtained in the different zones, since the values of z^+ were identified by the film thickness and not by the distance from the wall. Thus, the linear layer was measured in the base film only and its gradient cannot be used to calculate the velocity profile in the buffer layer, since the latter was measured only in disturbance waves. An attempt to clarify the difference between the velocity profiles in different zones could be made using the present data if one more assumption is made, namely, that the bubbles are uniformly placed along z-coordinate.

Under this assumption the following analysis can be performed. Every column (i.e., h_E value) in the 2D-distribution such as shown in Fig. 22 can be rearranged so that all the individual bubbles are sorted by velocity in ascending order and placed evenly over the range of z-values from 0 to h_E. Thus, for every h_E it is possible to construct a $U_x(z)$-dependence. The velocities of individual bubbles were collected into bins with length of 0.04 mm; the latter corresponds to radius of the smallest detectable bubble. The $U_x(z)$ dependencies for $Re_L = 520$ and $V_G = 35$ m/s are shown in Fig. 24(a). The obtained velocity profiles look plausible. The change in the wall shear stress with h_E roughly corresponds to the height of the line showing $U_x(h_E)$ at $z = 0.04$ mm. The wall shear stress grows with h_E, reaching maximum around $h_E = 0.5$ mm, then decreases and reaches saturated value around $h_E = 1$ mm, still remaining higher than that in the base film. This behaviour is given in better details by the three velocity profiles shown in Fig. 24(b). $h_E = 0.15$ mm corresponds to very thin films which are possible only in the base film zone. The velocity profile is approximately linear here. $h_E = 1.5$ mm corresponds to the crests of disturbance waves covered by the fast ripples. The wall shear stress here is about 1.5 times higher than that in the base film region and the velocity profile is definitely turbulent.

The range of intermediate h_E values around 0.5 mm most likely corresponds to the rear slopes of disturbance waves, since the front slopes are usually considered to be very steep and thus short. Under the rear slopes of disturbance waves the highest wall shear stress and the fastest velocity values for given distance from the wall are observed. It is interesting that in this area both fast and slow ripples are generated (Alekseenko et al., 2008), and the strongest wall shear stress may be related to ripples generation. An alternative explanation of the observed maximum wall shear is that the assumption on uniform spacing of the bubbles along z is incorrect here. That would denote that the bubbles are lifted further from the wall in this region due to internal flow towards the interface, and this flow may be responsible for ripples generation.

Definitely, there is a lot of speculation in the above considerations. We realise that we use a strong assumption, which is difficult to validate. Still, independently of its validity, there is a special zone under the rear slope of a disturbance wave which deserves further investigation using proper PIV experiments to obtain more detailed information about the velocity profile in the different zones.

Please cite this article as: D.B. Hann et al., Study of bubbles entrapped into a gas-sheared liquid film, International Journal of Multiphase Flow (2018), https://doi.org/10.1016/j.ijmultiphaseflow.2018.07.001

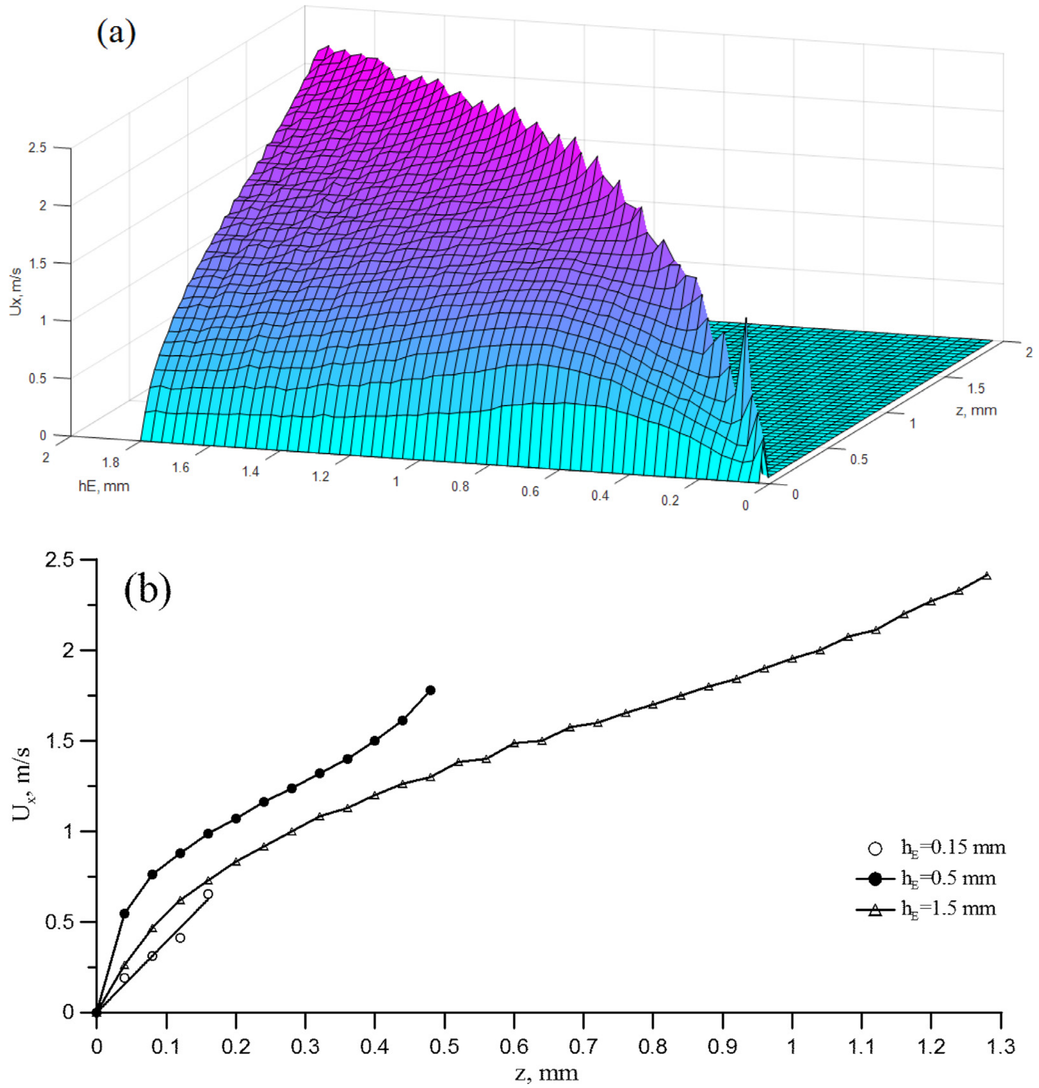

Fig. 24. The velocity profiles, $U_x(z)$, obtained for different values of h_E. (a) The whole set of obtained velocity profiles as a 3D-surface; (b) Three selected profiles in the base film ($h_E = 0.15$ mm), rear end of the disturbance waves ($h_E = 0.5$ mm) and top of the disturbance waves ($h_E = 1.5$ mm).

6. Conclusions

Gas bubbles entrapped by gas-sheared liquid film have been investigated using the BBLIF technique. This technique allowed us to study the bubbles simultaneously with the surface waves of different types and liquid droplets entrained from film surface into the gas core. Besides, this technique makes the identification of bubbles easier than common backlit visualisation. Qualitative studies of the mechanisms beyond bubbles creation and disappearance were supported by quantitative investigation of bubbles number, size and velocity distributions separately inside the disturbance waves and the base film. Based on these results, complete description of a bubble's evolution could be made as follows.

Entrapment of the bubbles. The majority of the bubbles are entrapped in the base film between the disturbance waves due to impacts of droplets depositing from the gas core under shallow angle ("furrow" impacts). This mechanism creates a lot of bubbles with sizes less or equal to the base film thickness. The exact physical processes leading to bubbles creation are still the subject for further investigation. Some of the new bubbles collapse immediately after creation during recovery of unperturbed shape by the film surface. The bubbles that survived travel inside the base film until the following disturbance wave overtakes them. A smaller number of bubbles characterised by significantly larger size may be entrapped in front of disturbance waves for two reasons: either due to impact of remnants of transitional liquid structures - liquid bags or liquid ligaments - which appear due to the deformation of fast ripple waves in the process of liquid entrainment or due to overturning of the fast ripple waves in front of disturbance waves.

Movement of the bubbles. The disturbance waves tend to capture the bubbles they overtake. On this reason the concentration of bubbles inside the disturbance waves increases significantly. The capability of a disturbance wave to hold bubbles is defined by the volume of fluid it contains. The volumetric density of the bubbles does not vary much within the same flow conditions but increases as square root of both gas and liquid flow rates. Based on the density data the regime borders of bubbles existence were estimated which qualitatively agree with the regime borders of liquid entrainment. This result is in agreement with qualitative observations on mechanisms of entrapment. The size distributions of bubbles normalised by the total number of bubbles are almost identical in the disturbance waves and the base film for the bubbles less than 0.5 mm. This similarity confirms that majority of the bubbles are created in the base film and accumulated by the disturbance waves. The disturbance waves show higher relative probabil-

Please cite this article as: D.B. Hann et al., Study of bubbles entrapped into a gas-sheared liquid film, International Journal of Multiphase Flow (2018), https://doi.org/10.1016/j.ijmultiphaseflow.2018.07.001

ity of larger bubbles, which are created just in front of disturbance waves.

Collapse of the bubbles. The bubbles move much faster inside the disturbance waves than inside the base film. Still, the bubbles are able to "escape" a disturbance wave or a slow ripple on the base film - probably, due to lower velocity of liquid under the humps of the wave than the interface velocity. If such a bubble gets into the film layer with thickness less than the bubble's size, it may collapse when trapped between the wall and the film surface, possibly due to action of gas shear. Other reasons of bubbles collapse are related to external perturbations caused by droplet impacts, collapses of other bubbles and severe flow oscillations under the fast ripples. We would expect that the number of bubbles grows with the distance from the inlet, since more and more impacting droplets create new bubbles in the base film. On the other hand, equilibrium bubble number will be achieved eventually after the base film is uniformly seeded by the bubbles with high enough concentration. In this case, impacting droplets would not only create new bubbles, but also destroy existing bubbles during the impact.

Study of liquid velocity profile using bubbles as tracers. Since the bubbles seem to follow the flow of surrounding liquid, an attempt to characterise the velocity profile in the liquid using bubbles as tracers was made. The velocity profile was obtained by measuring the maximum velocity of the bubbles entrapped by liquid film belonging to a narrow range of thickness. As a result, the velocity profile close to the wall was obtained for the base film only. An attempt to estimate the velocity profiles inside the base film and the disturbance waves was made assuming the uniform layout of the bubbles along the coordinate normal to the wall. It showed that the velocity profile is linear in the base film and turbulent inside the disturbance waves. The wall shear stress was found to be higher under the disturbance waves and reach the highest values under their rear slopes. Further work to measure the velocity profile below the wave is needed to fully understand the form of the flow since this analysis cannot resolve the distance between the wall and the bubble and the vertical velocity component of the bubbles.

In terms of the properties of the bubbles, further work should be aimed at the generalisation of the obtained results, by studying the process of bubbles entrapment in different conditions. In particular, it is interesting how the entrapped bubbles are affected by increasing viscosity and surface tension of working liquid, or by increasing downstream distance. Another promising direction of study is to investigate the effect exerted by presence of bubbles on the measurements of film thickness by various techniques, via simultaneous measurements of film thickness together with bubbles detection. In any of the future studies of the bubbles entrapped into a gas-sheared liquid film, improvement of spatial resolution is recommended.

Acknowledgements

This work was supported by the Engineering and Physical Sciences Research Council [grant number EP/K003976/1] through the Program Grant MEMPHIS and a joint project of Royal Society [IE150086] and Russian Foundation for Basic Research (15-58-10059-KO_a)

References

Alekseenko, S.V., Antipin, V.A., Cherdantsev, A.V., Kharlamov, S.M., Markovich, D.M., 2008. Investigation of waves interaction in annular gas-liquid flow using high-speed fluorescent visualization technique. Microgravity Sci. Technol. 20, 271–275.

Alekseenko, S.V., Cherdantsev, A.V., Markovich, D.M., Rabusov, A.V., 2014. Investigation of droplets entrainment and deposition on annular flow using LIF technique. At. Sprays. 24 (3), 193–222.

Alghoul, S., Eastwick, C., Hann, D.B., 2011. Droplet impact on shear-driven liquid films. At. Sprays. 21, 833–846.

Ashwood, A.C., Vanden Hogen, S.J., Rodarte, M.A., Kopplin, C.R., Rodríguez, D.J., Hurlburt, E.T., Shedd, T.A., 2015. A multiphase, micro-scale PIV measurement technique for liquid film velocity measurements in annular two-phase flow. Int. J. Multiphase Flow 68, 27–39.

Azzopardi, B.J., 1983. Mechanisms of entrainment in annular two phase flow. UKAEA Report AERE-R 11068.

Azzopardi, B.J., 1987. Observations of drop motion in horizontal annular flow. Chem. Eng. Sci. 42, 2059–2062.

Azzopardi, B.J., Teixeira, J.C.F., 1994. Detailed measurements of vertical annular two-phase flow-Part I: drop velocities and sizes. J. Fluids Eng. Trans. ASME 116, 792–795.

Barbosa Jr., J.R., Hewitt, G.F., Richardson, S.M., 2003. High-speed visualisation of nucleate boiling in vertical annular flow. Int. J. Heat Mass Transfer 46, 5153–5160.

Cao, Y., 2008. Hungarian algorithm for linear assignment problems (V2.3), Matlab file exchange.

Caroll, K., Mesler, R., 1981. Part II: Bubble entrainment by drop-formed vortex rings. AIChE J 27, 853–856.

Chanson, H., Gualtieri, C., 2008. Similitude and scale effects of air entrainment in hydraulic jumps. J. Hydraul. Res. 46, 35–44.

Cherdantsev, A.V., Hann, D.B., Azzopardi, B.J., 2014. Study of gas-sheared liquid film in horizontal rectangular duct using high-speed LIF technique: three-dimensional wavy structure and its relation to liquid entrainment. Int. J. Multiphase Flow 67, 52–64.

Cherdantsev, A.V., Hann, D.B., Hewakandamby, B.N., Azzopardi, B.J., 2017. Study of the impacts of droplets deposited from the gas core onto a gas-sheared liquid film. Int. J. Multiphase Flow 88, 69–86.

Cioncolini, A., Del Col, D., Thome, J.R., 2015. An indirect criterion for the laminar to turbulent flow transition in shear-driven annular liquid films. Int. J. Multiphase Flow 75, 26–38.

Cummings, P.D., Chanson, H., 1999. An experimental study of individual air bubble entrainment at a planar plunging jet. Trans IChemE 77, 159–164.

Dasgupta, A., Chandraker, D.K., Kshirasagar, S., Raghavendra Reddy, B., Rajalakshmi, R., Nayak, A.K., Walker, S.P., Vijayan, P.K., Hewitt, G.F., 2017. Experimental investigation on dominant waves in upward air-water two-phase flow in churn and annular regime. Exp. Therm. Fluid Sci. 81, 147–163.

Deane, G.B., Stokes, M.D., 2002. Scale dependence of bubble creating mechanisms in breaking waves. Nature 418, 839–844.

Deka, H., Ray, B., Biswas, G., Dalal, A., Tsai, P.-H., Wang, A.-B., 2017. The regime of large bubble entrapment during a single drop impact on a liquid pool. Phys. Fluids 29, 092101.

Fore, L.B., Dukler, A.E., 1995. The distribution of drop size and velocity in gas-liquid annular flow. Int. J. Multiphase Flow 21, 137–149.

Guo, Y., Lian, Y., 2017. High-speed oblique drop impact on thin liquid films. Phys. Fluids 29, 082108.

Hale, J., Akers, C., 2016. Deceleration of droplets that glide along the free surface of a bath. J. Fluid Mech. 803, 313331.

Hall Taylor, N., Hewitt, G.F., Lacey, P.M.C., 1963. The motion and frequency of large disturbance waves in ammlar two-phase flow of air-water mixtures. Chem. Eng. Sci. 18, 537–552.

Han, H., Zhu, Z., Gabriel, K., 2006. A study on the effect of gas flow rate on the wave characteristics in two-phase gas–liquid annular flow. Nucl. Eng. Design 236, 2580–2588.

Hann, D.B., Cherdantsev, A.,V., Azzopardi, B.J., 2015. Study of bubbles entrapment by gas-sheared liquid film using BB-LIF technique. 10th Pacific Symposium on Flow Visualization and Image Processing.

Hazuku, T., Takamasa, T., Matsumoto, Y., 2008. Experimental study on axial development of liquid film in vertical upward annular two-phase flow. Int. J. Multiphase Flow 34, 111–127.

Hewitt, G.F., Hall Taylor, N.S., 1970. Annular Two-Phase Flow. Oxford, Pergamon.

Hewitt, G.F., Jayanti, S., Hope, C.B., 1990. Structure of thin liquid films in gas-liquid horizontal flow. Int. J. Multiphase Flow 16, 951–957.

Hewitt, G.F., Roberts, D.N., 1969. Studies of two-phase flow patterns by simultaneous X-ray and flash photography. UKAEA Report AERE-M2159.

Hicks, P.D., Ermanyuk, E.V., Gavrilov, N.V., Purvis, R., 2012. Air trapping at impact of a rigid sphere onto a liquid. J. Fluid Mech. 695, 310–320.

Hidrovo, C.H., Hart, D.P., 2001. Emission reabsorption laser induced fluorescence (ERLIF) film thickness measurement. Meas. Sci. Technol. 12, 467–477.

Ishii, M., Grolmes, M.A., 1975. Inception criteria for droplet entrainment in two-phase concurrent film flow. AIChE J. 21, 308–318.

Israel, R., Rosner, D.E., 1982. Use of a generalized stokes number to determine the aerodynamic capture efficiency of non-stokesian particles from a compressible gas flow. Aerosol Sci. Technol. 2 (1), 45–51.

James, P.W., Hewitt, G.F., Whalley, P.B., 1980. Droplet motion in two-phase flow, In. Proc. Int. Topic. Meet. Nucl. React. Therm. Hydraul. 2, 1484–1503.

Kockx, J.P., Nieuwstadt, F.T.M., Oliemans, R.V.A., Delfos, R., 2005. Gas entrainment by a liquid film falling around a stationary Taylor bubble in a vertical tube. Int. J. Multiphase Flow 31, 1–24.

Kopplin, C.R., 2004. Local Liquid Velocity Measurements in Horizontal, Annular Two-Phase Flow M.Sc. Thesis. University of Wisconsin-Madison.

Korobkin, A.A., Ellis, A.S., Smith, F.T., 2008. Trapping of air in impact between a body and shallow water. J. Fluid Mech. 611, 365–394.

Matlab 2017b. Watershed transform, https://uk.mathworks.com/help/images/ref/watershed.html accessed 1/12/2017.

Mesler, R., 1976. A mechanism supported by extensive experimental evidence to explain high heat fluxes observed during nucleate boiling. AIChE J. 22, 246–252.

Miya, M., Woodmansee, D.E., Hanratty, T.J., 1971. A model for roll waves in gas-liquid flow. Chem. Eng. Sci. 26, 1915–1931.

Munkres, J., 1957. Algorithms for assignment and transportation problems. J Soc. Ind. Appl. Math. 5, 32–38.

Okawa, T., Shiraishi, T., Mori, T., 2008. Effect of impingement angle on the outcome of single water drop impact onto a plane water surface. Exp. Fluids 44, 331–339.

Pan, L.-M., He, H., Ju, P., Hibiki, T., Ishii, M., 2015. Experimental study and modeling of disturbance wave height of vertical annular flow. Int. J. Heat Mass Transfer 89, 165–175.

Pham, S.H., Kawara, Z., Yokomine, T., Kunugi, T., 2014. Detailed observations of wavy interface behaviors of annular two-phase flow on rod bundle geometry. Int. J. Multiphase Flow 59, 135–144.

Rodríguez, D.J., Shedd, T.A., 2004(a). Entrainment of gas in the liquid film of horizontal, annular, two-phase flow. Int. J. Multiphase Flow 30, 565–583.

Rodríguez, D.J., Shedd, T.A., 2004(b). Cross-sectional imaging of the liquid film in horizontal two-phase annular flow. In: Proceedings of ASME Heat Transfer/Fluids Engineering Summer Conference, July 11-15, 2004. Charlotte, North Carolina USA.

Schubring, D., Ashwood, A.C., Shedd, T.A., Hurlburt, E.T., 2010. Planar laser-induced fluorescence (PLIF) measurements of liquid film thickness in annular flow. Part I: methods and data. Int. J. Multiphase Flow 36, 815–824.

Thoraval, M.-J., Li, Y., Thoroddsen, S.T., 2016. Vortex-ring-induced large bubble entrainment during drop impact. Phys. Rev. E 93, 033128.

Thoroddsen, S.T., Etoh, T.G., Takehara, K., 2003. Air entrapment under an impacting drop. J. Fluid Mech. 478, 125–134.

Tran, T., de Maleprade, H., Sun, C., Lohse, D., 2013. Air entrainment during impact of droplets on liquid surfaces. J. Fluid Mech. 726, R3.

van der Meulen, G.P., 2011. Churn-annular Gas-Liquid Flows in Large Diameter Pipes. University of Nottingham.

van Nimwegen, A.T., Portela, L.M., Henkes, R.A.W.M., 2015. The effect of surfactants on air–water annular and churn flow in vertical pipes. Part 1: morphology of the air–water interface. Int. J. Multiphase Flow 71, 133–145.

Woodmansee, D.E., Hanratty, T.J., 1969. Mechanism for the removal of droplets from a liquid surface by a parallel air flow. Chem. Eng. Sci. 24, 299–307.

Worthington, A.M., 1908. A Study of Splashes. Longmans, Green, and Co., London.

Xiang, M., Cheung, S.C.P., Tu, J.Y., Zhang, W.H., 2014. A multi-fluid modelling approach for the air entrainment and internal bubbly flow region in hydraulic jumps. Ocean Eng. 91, 51–63.

Xie, Z., Hewitt, G.F., Pavlidis, D., Salinas, P., Pain, C.C., Matar, O.K., 2017. Numerical study of three-dimensional droplet impact on a flowing liquid film in annular two-phase flow. Chem. Eng. Sci. 166, 303–312.

Zadrazil, I., Markides, C.N., 2014. An experimental characterization of liquid films in downwards co-current gas–liquid annular flow by particle image and tracking velocimetry. Int. J. Multiphase Flow 67, 42–53.

Zadrazil, I., Matar, O.K., Markides, C.N., 2014. An experimental characterization of downwards gas–liquid annular flow by laser-induced fluorescence: flow regimes and film statistics. Int. J. Multiphase Flow 60 (2014), 87–102.

Zaidi, S.H., Altunbas, A., Azzopardi, B.J., 1998. A comparative study of phase Doppler and laser diffraction techniques to investigate drop sizes in annular two-phase flow. Chem. Eng. J. 71, 135–143.

Please cite this article as: D.B. Hann et al., Study of bubbles entrapped into a gas-sheared liquid film, International Journal of Multiphase Flow (2018), https://doi.org/10.1016/j.ijmultiphaseflow.2018.07.001